Simultaneous rupture propagation through fault bifurcation of the 2021 Mw7.4 Maduo earthquake

Shengji Wei[1,2*], Hongyu Zeng[2], Qibin Shi[1], Jihong Liu[3], Heng Luo[4], Wanlin Hu[2], Yu Li[5,6], Weitao Wang[5], Zhangfeng Ma[2,7], Jing Liu-Zeng[8], Teng Wang[4]

1. Earth Observatory of Singapore, Nanyang Technological University, Singapore
2. Asian School of the Environment, Nanyang Technological University, Singapore
3. School of Geosciences and Info-Physics, Central South University, Changsha, China
4. School of Earth and Space Sciences, Peking University, Beijing, China
5. Institute of Geophysics, China Earthquake Administration, Beijing, China
6. China Earthquake Networks Center, China Earthquake Administration, Beijing, China
7. School of Earth Sciences and Engineering, Hohai University, China
8. School of Earth System Science, Tianjin University, Tianjin, China

Abstract

Fault geometric complexity plays a critical role in earthquake rupture dimension. Fault bifurcations are commonly observed in earthquake geology, yet, robust kinematic rupture processes on bifurcated fault branches are largely missing, limiting our understanding of rupture dynamics and seismic hazard. Here, we holistically study the fault geometry and bilateral rupture of the 2021 Mw7.4 Maduo, China earthquake, that shows clear fault bifurcation near its eastern terminal. We integrate space geodesy imaging, back-projection of high-frequency teleseismic array waveforms, multiple point source and finite fault inversions, and constrain in detail the rupture process, in particular, through its fault bifurcation. Our models reveal a stable rupture speed of ~2.5 km/s throughout the entire rupture and a simultaneous rupture through fault branches bifurcated at 20°. The rupture on bifurcated faults radiated more high-frequency waves, especially from the stopping phases. The stopping phase on the southern branch likely stopped the rupture on the northern branch.

Plain Language Summary

Earthquake is produced by sudden shear dislocation across the fault. The geometric complexity of fault structure, such as bend, step-over, branching and bifurcation, play important roles in determining the final rupture dimension

(hence the magnitude) of the earthquake, as they can easily produce stress heterogeneity on the faults. Although geological and recent space geodetic observations have well-recorded the fault geometry complexity, detailed spatial and temporal evolution of rupture through such fault segments, especially fault bifurcations, are rarely well-imaged. In this study, we integrate broadband seismic waveform and geodetic observations for the 2021 Mw7.4 Maduo earthquake in China, and process and model them with a set of tools, to produce a high resolution rupture model for the earthquake. The preferred model reveals a near constant rupture speed of 2.5 km/s throughout the entire rupture, and resolves the detailed rupture process through the bifurcated fault segments at its eastern terminal, where the termination of the rupture on the southern branch stopped the rupture on the northern branch.

Key Points

1. Geodetic imaging, back-projection, multiple point source and finite fault inversions are conducted for the Maduo earthquake
2. We show a stable rupture speed (~2.5km/s) of the entire rupture and a simultaneous rupture through bifurcated fault branches.
3. The stopping phase on the southern branch likely stopped the rupture on the northern branch.

Introduction

Fault bends, branches, and step-overs play critical roles in the nucleation, propagation, and termination of earthquake ruptures [*Ji et al.*, 2003; *King and Nábělek*, 1985; *Qiu et al.*, 2016; *Wesnousky*, 2006]. Fault branching and bifurcation are commonly observed for strike-slip earthquakes in fault mapping [e.g. *Sieh et al.*, 1993] and more recently in high-resolution space geodesy images [e.g. *Wei et al.*, 2011]. To explain these observations, structure evolution models [*Wesnousky*, 1988; 2008], theorical analysis [*Poliakov et al.*, 2002], dynamic simulation models [*Kame et al.*, 2003], as well as lab experiments[*Templeton et al.*, 2009] have been proposed. It has been shown that prestress conditions, rupture speed, and bifurcation angle all impact rupture evolution through fault branching and bifurcation [*Aochi et al.*, 2002; *Douilly et al.*, 2020; *Duan and Oglesby*, 2007; *Kame et al.*, 2003; *Poliakov et al.*, 2002]. These theorical and numerical modeling results show a wide spectrum of rupture scenarios. However, to date, to the best of our knowledge, the details of kinematic rupture processes of such fault bifurcation and branching have not been reported. This may be partially accounted for by the fact that the slip on these faults is relatively small compared with the largest slip patches of the rupture, and seismological inversions are usually dominated by the larger slip patches, unless very near-fault seismic observations are available [*Ji et al.*, 2003].

The left-lateral strike-slip Mw7.4 Maduo earthquake occurred on May 21st, 2021, rupturing the near E-W oriented JiangCuo fault, which is located within the Bayan Har block [*Zhan et al.*, 2021] in the northeastern Tibetan Plateau (Fig.1b).

The earthquake was well-recorded in space geodetic images [*He et al.*, 2022; *J Liu et al.*, 2022] and nearby static [*M Wang et al.*, 2022a] and high-rate GPS offsets [*Gao et al.*, 2021]. Earlier reports of the earthquake show that this was a bilateral rupture, which propagated ~80 km to both sides of the epicenter [*He et al.*, 2022; *Ren et al.*, 2022; *S Wang et al.*, 2022b]. While [*K Chen et al.*, 2022] derived a stable rupture speed of ~2.5km/s for the entire rupture, [*Zhang et al.*, 2022] and [*Yue et al.*, 2022] reported a supershear speed for rupture towards the east. Although various analyses have been reported for the earthquake, a comprehensive investigation of the rupture process is still missing to resolve the kinematic rupture details of the earthquake, especially at its eastern end that shows clear fault bifurcation but reported with different rupture speeds. To constrain the rupture details of the earthquake, here we adopt various data processing techniques and kinematic inversion methods that cover a wide range of observations. We pay special attention to the fault bifurcation and its seismic wave radiation, thus aiming to shed new light on earthquake physics.

Geodetic observations

We process Sentinal-1 and Advanced Land Observation Satellite-2 (ALOS-2) SAR data (Table S1) to derive 11 surface deformation images through DInSAR (differential interferometric SAR)[*Gabriel et al.*, 1989], POT (pixel offset tracking)[*Michel et al.*, 1999], MAI (multiple aperture interferometry)[*Bechor and Zebker*, 2006], and/or BOI (burst overlap interferometry)[*Grandin et al.*, 2016] methods (Fig.S1). These images provide high-quality and comprehensive spatial coverage of the surface deformation produced by the earthquake. We then use them to calculate the 3D co-seismic displacement with the Strain Model and Variance Component Estimation method[*J Liu et al.*, 2019b; *J-H Liu et al.*, 2017] (**Supplement text-1**). The high-resolution 3D surface deformation shows sharp offsets across the fault, thus the surface rupture, continuously along the near E-W oriented Jiangcuo fault (Fig.1b and Fig.S2), which agrees well with the surface rupture mapping from field surveys [*Ren et al.*, 2022]. The total surface rupture length is ~160 km, ~60 km longer than that predicted from empirical relationships [*Leonard*, 2010; *Wells and Coppersmith*, 1994], suggesting a relatively shallow rupture of the earthquake. The coseismic deformation is dominated by left-lateral strike-slip motion (Fig.1a), and shows at least five primary step-overs or fault bends (strike change $> 10°$) and one fault bifurcation. The refined hypocenter of the mainshock [*W Wang et al.*, 2021] is located in the middle of the surface rupture trace very close to one of the primary fault step-overs, where stress concentrations usually nucleate an earthquake rupture [*King and Nábělek*, 1985]. Interestingly, the epicenter is co-located with the intersection between the Yellow River and the ruptured JiangCuo fault (Fig.2a), although their relationship is not yet clearly understood. Larger surface deformation is observed to the east of the epicenter, and therefore a stronger rupture directivity effect is expected toward the east. Coseismic offsets are clearly observed across the bifurcated fault branches near its eastern terminal (Fig.1a).

Fault geometry and finite fault inversion

We use the geodetic observations and the relocated aftershocks [*W Wang et al.*, 2021] to define the geometry of rectangular fault segments that will be used in the finite fault model (FFM) inversion. Ten fault segments are needed to mimic the first-order strike variations due to bending and bifurcation, as shown in the geodetic observation (Fig.1a and Fig.2a). These ten segments are sub-vertical faults, as aftershocks are distributed quite close to the surface rupture trace (Fig.2b), and the E-W deformations across the fault are nearly symmetric (Fig.1b). Aftershocks are located mostly to the north of surface rupture at fault segments 1-6 while aftershocks are distributed primarily to the south of surface rupture at fault segments 7-10. Based on this relative location between seismicity and surface rupture trace, we set the dipping direction of fault segments 1-6 and 7-10 towards north and south, respectively (Fig.2). Note, that the seismic stations used in earthquake relocation study are distributed quite uniformly in the source region [*W Wang et al.*, 2021]. Therefore, we can rule out the systematic location bias between the seismicity to the west and east of the epicenter. Geodetic-only inversions can then be conducted to determine the dip angle of each fault segment (Table S2).

Based on this fault geometry, we jointly invert geodetic data, nearby high-rate Global Positional System (GPS) waveforms, regional broadband waveforms and teleseismic body waves using a finite fault inversion method [*Ji et al.*, 2002] to recover the kinematic rupture history and slip distribution on the fault segments (**Supplement text-2**). We divide the rectangular fault segments into 3 km $\times$ 2 km patches, and invert for the slip amplitude, slip direction, rupture time and rise time on each patch. A Laplacian smoothing algorithm is applied for the slip distribution during the inversion. High-quality nearfield geodetic and high-rate GPS observations greatly suppress the trade-offs between the parameters in the inversion.

Our preferred FFM is presented in Fig.2b in a map view and in Fig.3 as a depth view along the strike. This model produces excellent fits to both seismic waveforms (Fig.S3-5) and static surficial deformations (Fig.S6-8), suggesting a reliable model resolution. Most of the slips are distributed at the depth shallower than 8 km except for S5 and S6, where slips are as deep as 15 km. Interestingly, the distribution of the aftershocks also shows a gap at S5 and S6 (Fig.2b and Fig.3d), indicating the rupture released most of the stress accumulated in the entire seismogenic zone, which has a depth of ~15 km. On the other segments, where the seismogenic zone is only partially ruptured, aftershocks are much denser, and distributed in the depth range of 5-15 km, showing a clear complementary feature with the coseismic slip distribution (Fig.3d), similar to that observed for other strike-slip earthquakes (e.g., [*Wei et al.*, 2011]). The aftershocks were most likely triggered by down-dip post seismic slip and Coulomb stress change imposed by coseismic slip. Therefore, slip deficit happens both at shallow [*Jin and Fialko*, 2021] and at greater depths, that is, at the upper and lower bounds of the seismogenic zone. The equivalent moment tensor of the FFM shows relatively small non-double-couple component (Fig.3b), which is highly similar to that from multiple point source solution (see next section).

Our equivalent moment tensors are more similar to the GCMT solution, including the Mw, but much more different from the W-phase solution, in which the east-west oriented fault plane has a shallower dip angle (67°) and quite strong normal faulting component in rake (-40°). It appears that a reliable FFM of Maduo earthquake provides an independent verification to the global moment tensor solutions.

There are substantial slip distributions on the two branches of the bifurcated fault, where the moment magnitude of the northern branch (S7-8, Mw6.8) is slightly larger than that on the southern branch (S9-10, Mw6.7). The sizable and comparable moment distribution on the two branches is a key feature that allows robust resolution on their ruptures. The waveform observations on high-rate GPS station HSHX exhibit a clear frequency-dependent feature that the rupture from the bifurcated branches (S7-10) produced more high-frequency seismic waves than that from earlier ruptures (S1-6) (Fig.4). HSHX station is located at almost the same distances away from S4-10 (Fig.2b), therefore the geometric spreading induced attenuations at HSHX are similar for ruptures on these fault segments. If we assume pure strike-slip motion uniformly distributed on these fault segments, we would expect stronger seismic waves from S4-6 as the azimuth of HSHX is closer to the strongest SH-wave radiation direction of S4-6. Indeed, in the displacement waveforms, which are dominated by low-frequency energy, seismic waves excited from S1-S6 show larger amplitudes than those from S7-10, as shown in the synthetic waveform decompositions (Fig.4). However, in velocity waveforms, in which higher-frequency features are presented, the waveform amplitudes from S7-S10 are larger than those from S1-S6. This suggests that S7-10 radiated more high-frequency waves than those on the other fault segments. Note that the displacement waveforms are dominated by the periods of 10 - 20 s, while the velocity waveforms show stronger energy at 5 - 10 s. We did not fit the N-S velocity waveform as good as the E-W component for the rupture from S7-10 (highlighted by circles in Fig.4). This portion of the waveform shows more high frequency energy in the N-S component than the E-W component. This larger misfit to the higher frequency waveform is likely because our FFM inversion is dominated by relatively low frequency energy in the observations.

Multiple point source solution

The key rupture characteristics of the Maduo earthquake are further confirmed at the intermediate frequency bands, with a multiple point source (MPS) inversion method [*Q Shi et al.*, 2018] using high-rate GPS waveforms, regional broadband waveforms, and teleseismic body waves (Fig.S9) (**Supplement text-3**). An MPS solution usually uses 2-10 pure dislocation point sources to approximate the complex fault geometry and the rupture process of a large earthquake ([e.g. *Duputel et al.*, 2012]). Compared with a finite fault model, a smaller number of MPS parameters can resolve the most robust earthquake rupture features at 0.2 Hz and lower frequencies for the Maduo earthquake. In this frequency range, we find that 6-point sources (M1-M6, table S3, Fig.S10-13) are needed

to adequately approximate the first order geometry and rupture complexity of the earthquake.

Our preferred MPS solution is presented as beach balls in map view (Fig.2) and depth profiles (Fig.3), with M1-2 and M3-6 located to the west and east of the epicenter, respectively. Uncertainty distributions of the solution (Fig.S10-11) show that the location, starting time, length and shape of the source time function, and focal mechanism parameters are well resolved, mostly owing to the constraints of nearby high-rate GPS observations. Fig.S12 presents the decomposition of synthetics from each sub-events in fitting the closest high-rate GPS stations, which demonstrates the sensitivity and variation of the contributions from different stations. The centroid depths of M3 (7.8 km) and M4 (7.8 km) correspond to deep ruptures on fault segments S4-6, while M1, M2, M5, and M6 (3-6 km) indicate relatively shallow ruptures. This is highly consistent with the FFM slip distribution (Fig.3). The summation of source time functions from the MPS solution also highly resembles the FFM moment-rate function, except for several high-frequency features, which is expected, as we use lower-frequency waves in the MPS inversion. Interestingly, M5 and M6 are located on the northern and southern branches of the fault bifurcation, respectively. The strike of E-W oriented fault plane of M5 is ~10 degrees counter-clockwise to the strike of M6 (Fig. S11), roughly consistent with the strike difference between the two fault branches. The source durations of M5 and M6 are shorter than those of the other sub-events (Fig.S10b), as also shown in the waveform decomposition in fitting the closest high-rate GPS data, where M5 and M6 show sharper pulse in fitting the later portion of E-W component at HSHX station (Fig.S12). This shorter source time function feature is in line with more high-frequency energy radiation from the bifurcation rupture as revealed by the FFM model and the following back-projection analysis.

Back-projection rupture process imaging

To resolve its high frequency radiation and the rupture speed of the Maduo earthquake independent from FFM and MPS solutions, we perform a MUltiple SIgnal Classification (MUSIC) back-projection (BP) analysis[*Meng et al.*, 2011; *Zeng et al.*, 2020] using high-frequency (0.3-1.0 Hz) teleseismic P-waves recorded by the European array (EU) and Australian array (AU) (**Supplement text - 4**). To take into account the potential impact of the 3D source-side velocity structure on the travel time, we apply a path calibration algorithm using the arrival times of mainshock and other nearby events, which was proved to be necessary for more accurate BP analysis [*Zeng et al.*, 2022]. The effectiveness of the calibration is verified by applying it to the BP analysis of the $M > 5$ aftershocks. We compare the differences between the BP locations and the refined epicenter locations for these events [*W Wang et al.*, 2021]. Note that our calibration events include the earthquakes away from the mainshock rupture zone (Fig.S14), such selection was shown to be more accurate for travel time error interpolation [*Zeng et al.*, 2022]. After trying different groups of calibration events, it appears that we need to use different calibration event combinations

to obtain high consistency between the calibrated BP locations and the refined epicenters for the events located to the east and west of the mainshock epicenter, respectively (Fig.S14-15). This calibration strategy works well for the EU and AU arrays, as they can only resolve the rupture directivity towards west and east, respectively, likely due to the Doppler effect from rupture directivity. We consider the average difference between the BP locations and epicenters as the location uncertainty of BP results, which is 7.5 km for AU array and 4.5 km for the EU array.

Using this path-calibrated BP method, we derive the spatial and temporal evolution of the mainshock rupture using EU and AU arrays. The results are presented as location of high-frequency radiators colored by their timing (Fig.2a). BP results from the EU array reveal only the rupture directivity towards the west, and the results from the AU array show only rupture directivity towards the east. The locations of the BP results are mostly less than 10 km away from the surface rupture, suggesting reliable solutions. The location of the large amplitude high-frequency radiators are highly correlated with the fault bends or step-overs (Fig.2a), which also mark the boundaries of fault segments (Fig.3c). This is because stress is usually concentrated at fault kinks and bends [*King and Nábělek*, 1985], where coseismic slip distribution shows larger gradients (e.g., Fig.3d). Such complementary feature between BP result and slip distribution also presents in the moment-rate vs BP power plot (Fig.3a), where the peaks of BP power always locate at the edges of moment-rate peaks.

With the timing and location of the high-frequency radiators, the rupture speed of the earthquake can be derived (Fig.5), which shows a speed of 2.4 km/s towards the west and of 2.5 km/s towards the east. These rupture speeds are quite stable throughout the rupture and highly consistent with the result from FFM and MPS inversions. Given that the shallow part (<6 km, where most of the slip took place) of the crust has a shear wave (Vs) velocity of 2.7 km/s [*L Zhu and Helmberger*, 1996], these rupture speeds are roughly 90% of Vs speed, that is, of the Rayleigh wave speed. Note, that to the west of the fault bifurcation, the BP results show a gap that almost overlaps with the gap in the aftershock seismicity (Fig.3). The coseismic rupture of this fault segment is deeper, as shown on fault segment S6 in the FFM, and smoother, as shown in the waveform decomposition (Fig.4), than the rupture on the other fault segments. Such a smoother rupture could be explained as more uniform stress distribution and/or smoother fault geometry [*Z Shi and Day*, 2013]. As the rupture propagated through the junction of bifurcation, high-frequency radiators started to appear on both fault branches, with their amplitudes increasing gradually as the rupture propagated on each of the fault branch (Fig.2a). Enhanced higher-frequency radiation from the bifurcated fault branches (segments S7-10) is consistent with the waveform decomposition analysis of the high-rate GPS data recorded at HSHX station (Fig.4 and Fig.S12). But note, that GPS velocity waveforms are dominated by the ~0.2 Hz energy, while the BP results are derived at ~1.0 Hz. It is interesting to see that the largest amplitude of high-frequency radiators on the bifurcated fault branches are located at the end of each fault branch

(Fig.2a inset). The timings of these peaks are also consistent with the end of the rupture time, as shown in both the MPS source time function and FFM moment-rate function (Fig.3a). Therefore, we propose that the large amplitude high-frequency radiators on each fault branch were produced by the stopping phase of the rupture [*Savage*, 1965]. Rupture on the southern branch (S10) stopped ~5s earlier than the rupture on the northern branch (S8) (Fig.3a and Fig.5b). As shown in the surface deformation image (Fig.2a), the distance between the rupture tips on the two fault branches is ~15 km, which corresponds to ~5s for the S-wave of the stopping phase to travel between the two fault tips. It is therefore likely that the stopping phase on the southern branch (S10), which produced negative Coulomb stress change on the northern branch (S8), therefore stopped the rupture on S8. From the timing and location of the BP results, we show that the rupture propagated simultaneously on the two branches of the bifurcation.

Discussion

Multiple datasets and results derived from various inversion methods show that the 2021 Maduo earthquake ruptured simultaneously on the two branches of the fault with a branching angle of ~20°. However, numerical simulations suggest that simultaneous rupturing on both fault branches is usually difficult where the branching angle is narrow, due to strong stress interactions between faults [*Aochi and Fukuyama*, 2002; *Kame et al.*, 2003]. The dynamic stress interaction (or dynamic rupture weakening) plays an important role during earthquake ruptures. Given the stress shadow imposed by the rupture on the other fault branch, rupture through a fault bifurcation that has a narrow branching angle is most likely be simultaneous. Suppose that one of the fault branches ruptures earlier; then the Coulomb stress change on the other fault segment will prohibit its rupture. Only when the ruptures propagate simultaneously through the two fault branches (e.g., Fig.5c), back and forth slip of the fault segments could be avoided. Because the two sides of the wedge block have opposite slip directions (Fig.5c), the final dislocation of this block is smaller than that to the north and south of the block (e.g., Fig.1a inset). Numerical simulations also suggest that a simultaneous rupture is promoted when the friction coefficients are low [*Aochi et al.*, 2002]. However, we observe more high-frequency radiation from the bifurcated fault branches, which indicates rougher fault friction. More high-frequency energy released on the branched faults could also be an indication of more energy dissipation, which could eventually lead to the termination of the rupture. Also note, that the bifurcated fault branches are located within slightly higher mountain ranges, suggesting the rupture could have propagated from one geological unit to another [*Ren et al.*, 2022], which could also be a reason for different fault friction. The rupture speed of the Maduo earthquake was quite stable around 2.5 km/s, which is in contrast with supershear rupture speed derived from the other BP analysis [*Yue et al.*, 2022; *Zhang et al.*, 2022]. The primarily reason for this discrepancy could be that we applied travel time path calibrations (see more details in [*Zeng et al.*, 2022]) but the other BP studies did not. The rupture did not slow down at the bends and

step-overs. This is because all bends/step-overs are releasing bends/step-overs, therefore normal stress decreased when rupture propagated through them, and facilitating the rupture pass-through. Fault bifurcations with narrow branching angle are quite common for strike-slip earthquakes (Fig.S16). The number of fault segments and fault segment length of the Maduo earthquake, including the bifurcated branches, fit well with statistics from [*Klinger*, 2010]. We therefore suggest that such simultaneous ruptures of the bifurcated fault branches could be common during strike-slip earthquakes. Dynamic simulations have to take into consideration complex fault geometry, specific stress conditions, and frictional heterogeneities to properly estimate the relationship between rupture through multiple fault segments.

Data Availability Statement

The seismic data used in this study can be downloaded from the II (https://doi.org/10.7914/SN/II) and IU (https://doi.org/10.7914/SN/IU) networks in Incorporated Research Institutions for Seismology (IRIS) through its Wilber3 service (http://ds.iris.edu/wilber3/find_event). Seismic and geodetic datasets used in the inversion can also be downloaded from NTU data repository: https://doi.org/10.21979/N9/NOKYXP.

Acknowledgement

This research was supported by Singapore MOE project (MOE2019–T2–1–182) and the Earth Observatory of Singapore via its funding from the National Research Foundation Singapore and the Singapore Ministry of Education under the Research Centres of Excellence initiative. This work comprises EOS contribution number 445.

Author contributions

S.W. conceived and supervised the project, conducted finite fault inversion and wrote the manuscript, Y.Z. conducted back-projection, Q.S. conducted multiple point source inversion, J.L. conducted geodetic data processing and derived 3D surface deformation, H.L. performed geodetic data processing and downsampled the data, W.H. designed tectonic map and provided geologic information, Y. L. processed high-rate GPS data, W.W. processed regional broadband data, Z.M. processed part of the geodetic data, J.L-Z provided geologic information and revised the manuscript, T.W. provided geodetic information and revised the manuscript. All authors discussed the results and interpretations, and contributed to the manuscript.

Competing interests

The authors declare no competing interests.

Figures and Captions

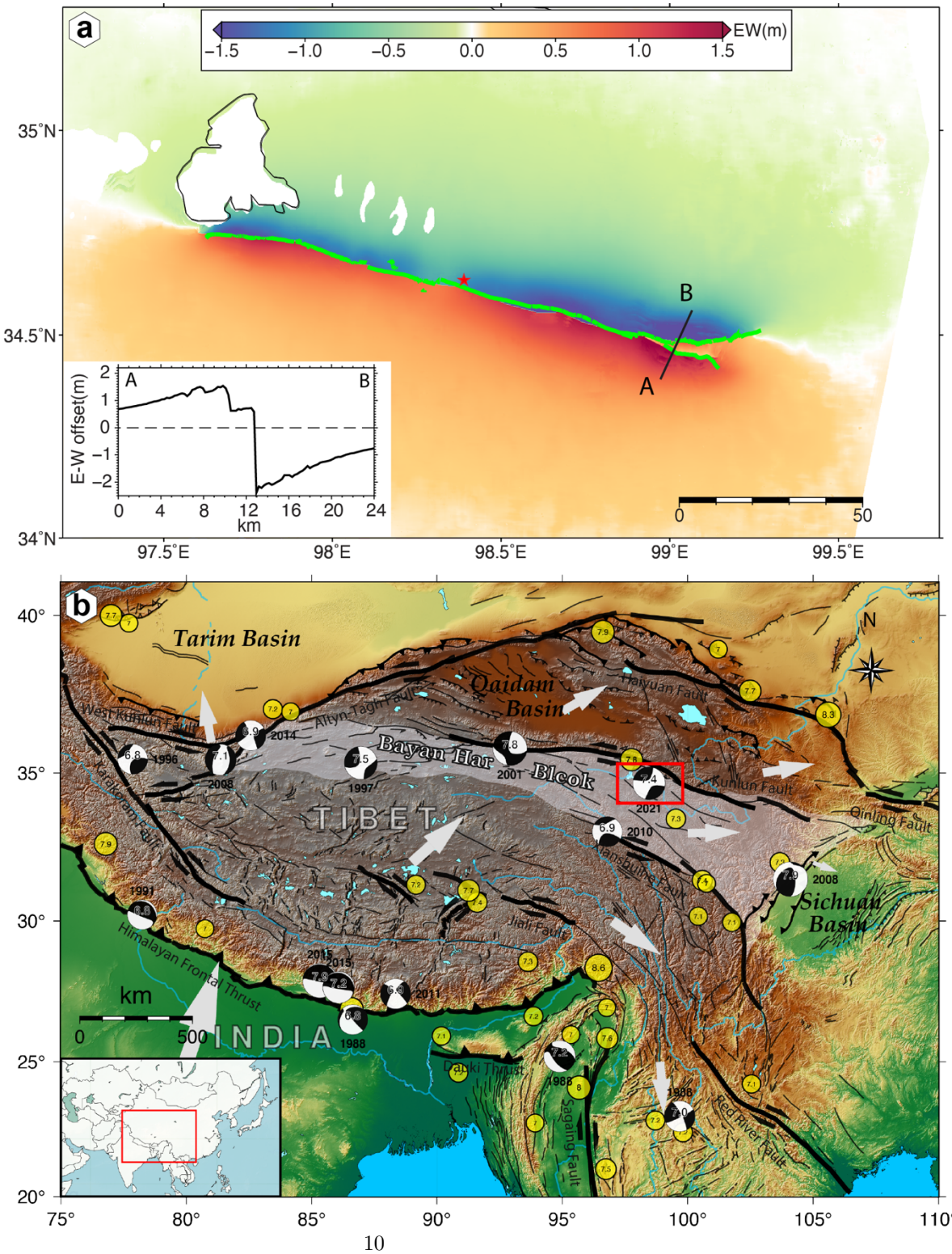
a
EW(m)
−1.5
−1.0
−0.5
0.0
0.5
1.0
1.5
35°N
34.5°N
34°N
97.5°E
98°E
98.5°E
99°E
99.5°E
B
A
E-W offset(m)
km
0
50
b
Tarim Basin
Qaidam Basin
Haiyuan Fault
Altyn-Tagh Fault
West Kunlun Fault
Bayan Har Block
TIBET
Kunlun Fault
Qinling Fault
Sichuan Basin
Longmenshan Fault
Xianshuihe Fault
Jiali Fault
Himalayan Frontal Thrust
INDIA
Dali Thrust
Sagaing Fault
Red River Fault
N
40°
35°
30°
25°
20°
75°
80°
85°
90°
95°
100°
105°
110°

Figure 1. Regional tectonics and surface deformation. (a) E-W component of the 3D surface deformation derived from space geodetic observations. The green lines indicate the surface rupture mapped by [*Ren et al.*, 2022]. The inset shows the offset along the profile A-B. (b) Regional tectonics with major strike-slip and thrust faults indicated by the heavy black lines. Earthquake moment tensor for Mw>6.5 earthquakes in 1990 – 2022 are shown as beach balls, along with magnitude and year of the event. Historical M>7.0 earthquakes in the last 100 years are displayed as yellow circles. 2022 Mw7.4 Maduo earthquake is highlighted by the red rectangle, defined as the same area as in (a).

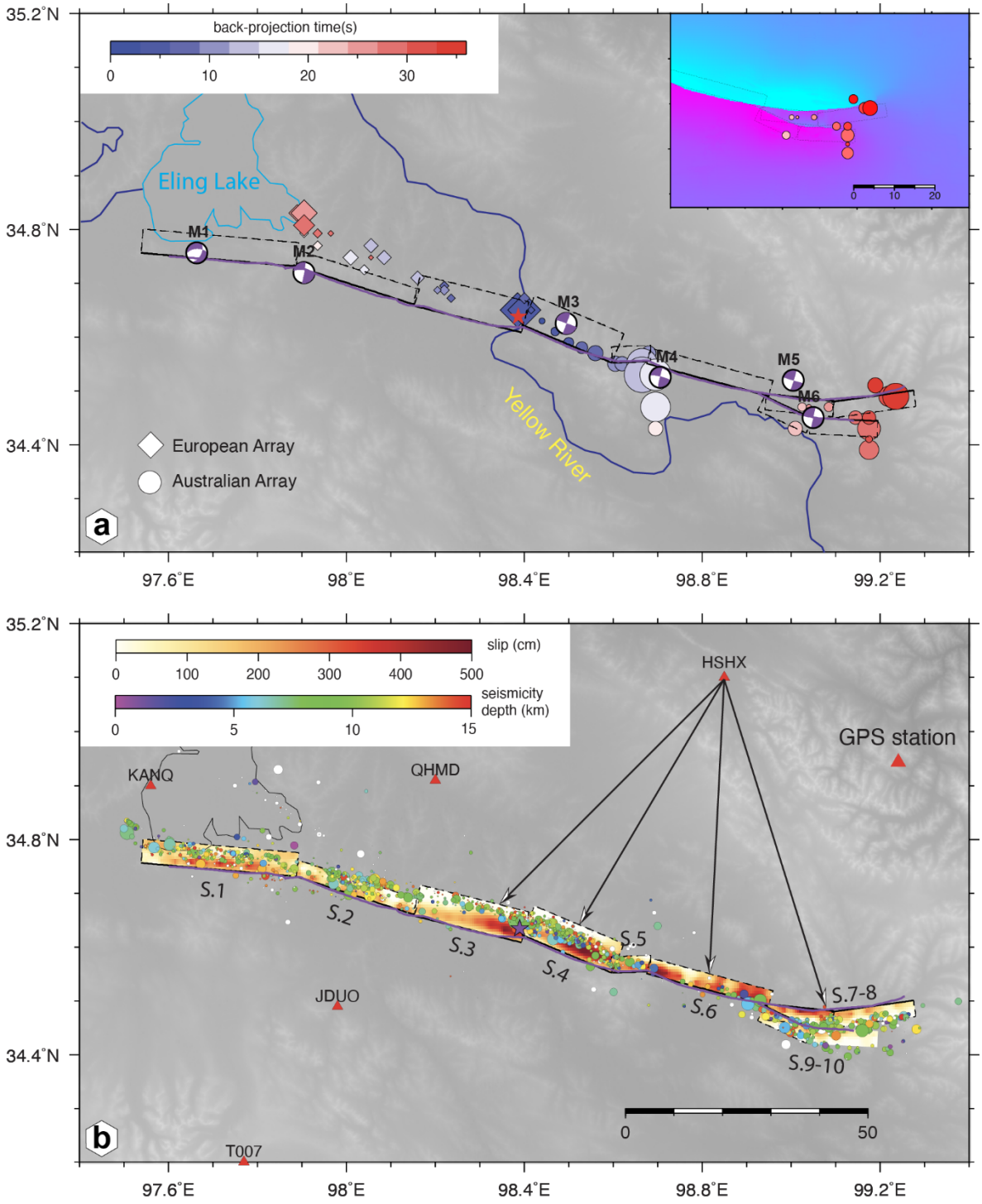
back-projection time(s)
0
10
20
30
Eling Lake
M1
M2
M3
M4
M5
M6
Yellow River
European Array
Australian Array
a
35.2°N
34.8°N
34.4°N
97.6°E
98°E
98.4°E
98.8°E
99.2°E
slip (cm)
0
100
200
300
400
500
seismicity
depth (km)
0
5
10
15
HSHX
GPS station
KANQ
QHMD
JDUO
T007
S.1
S.2
S.3
S.4
S.5
S.6
S.7-8
S.9-10
0
50
b

Figure 2 (a) Map view of the BP results derived from European Array (diamond) and Australian array (circles). Surface rupture trace is indicated by the purple line. Rectangles show the surface projection of the fault segments used in FFM inversion. MPS solutions are indicated by beach balls with the sub-event ID. The inset shows the E-W component of the 3D surface deformation at the eastern terminal of the rupture, along the BP result. (b) Map view of the slip model, displayed with the relocated aftershocks [*W Wang et al.*, 2021] that are colored by their depth. Circles are proportional to the magnitude of the aftershock. Fault segment numbers used in FFM inversion are indicated as S1-10. Triangles indicate the high-rate GPS stations that are used in the FFM inversion. The arrows connected to station HSHX roughly show the distance differences from the station to various fault segments.

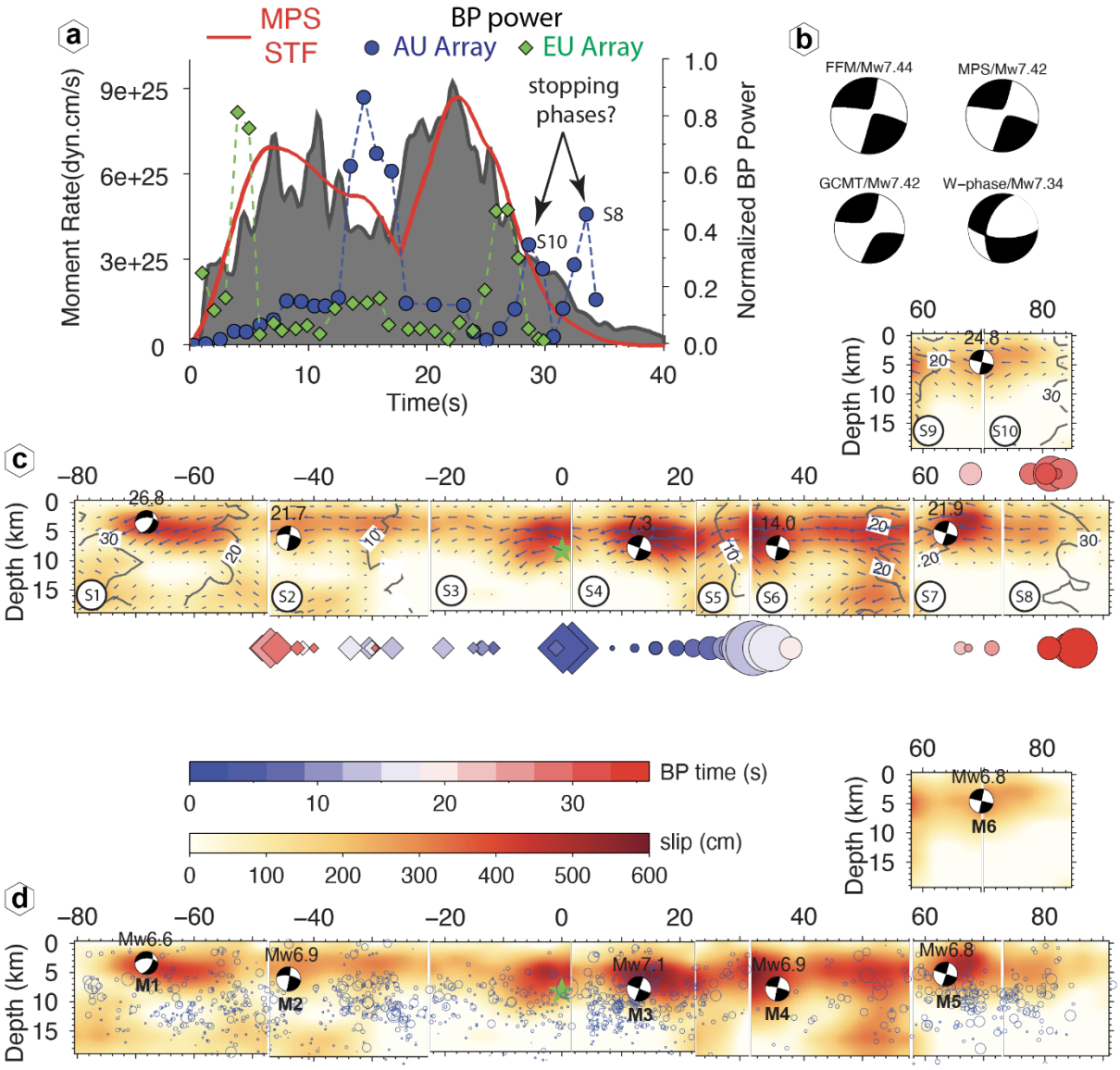

Figure 3, dynamic rupture models. (a) Shaded curve represents the moment-rate function of FFM, summed source time function of MPS solution is indicated by the red line, and BP power from Australian array (circle) and European array (diamond). (b) Equivalent moment-tensors of FFM and MPS solutions, along with that reported from GCMT and W-phase catalogs. (c) Depth profile of the rupture model with the green star shows the hypocenter. Segment numbers are indicated in the lower left corner of each segment (see Fig.2 for their map view). Blue arrows show the rake angle of each sub-fault and contour lines indicate the rupture time. The beach balls represent the MPS solution with

the number above indicating the centroid time of the sub-event. BP results are displayed below, with the same legend as shown in Fig.2. (d) Depth profile of slip model displayed with the aftershocks (blue open circles) and MPS solution (beach balls). The moment magnitude (above) and sub-event ID (below) are shown with the beach balls.

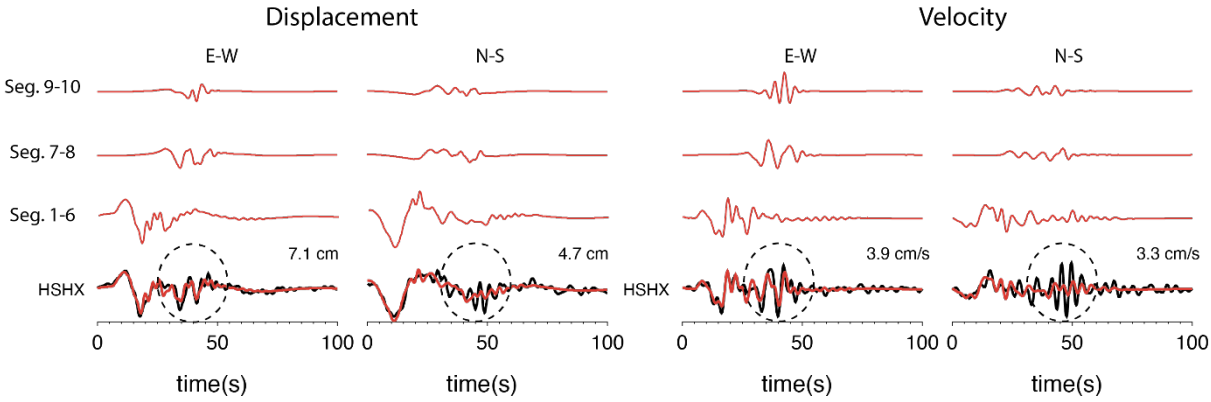

Figure 4. Waveform fits of the horizontal components for high-rate GPS station HSHX in displacement (left) and velocity (right), with the synthetics in red and data in black. All the waveforms are filtered to 0.02 – 0.4 Hz. Peak amplitude of the data is indicated at the end of each waveform pair. Synthetic waveforms are decomposed into the contributions from Seg.1 - 6, Seg.7 - 8 and Seg. 9 – 10. Dashed circles highlight the waveform segments that show different relative amplitude to the earlier rupture between displacement and velocity waveforms.

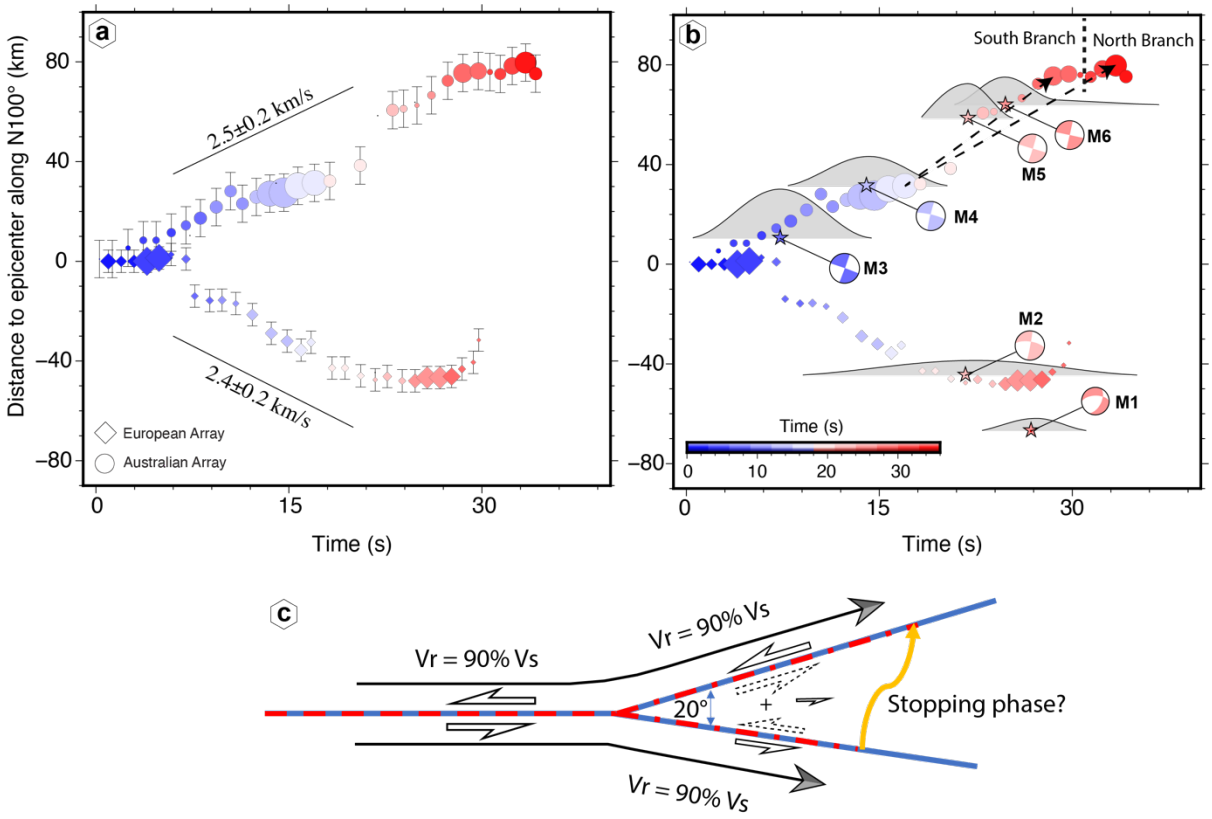

Figure 5. Rupture speed estimation from back projection and MPS inversion results. (a) Spatial and temporal distribution of the high frequency radiators derived from European array (diamonds) and Australian array (circles), plotted relative to the epicenter location and time. Two straight lines indicate the approximated averaged rupture speed towards east and west of the epicenter. Vertical bars are the spatial errors of the BP results (see **Supplement** for more details). (b) Overlaps of the BP and MPS results. Stars are the centroid location of subevents in MPS solution. Shaded curves represent the source time function of each subevent, both the stars and beach balls are colored by the centroid time. The dashed line separates the high frequency radiators from the north and south branches of the bifurcation rupture. (c) A schematic cartoon shows the rupture (red lines) propagation through the fault bifurcation. The sandwiched/wedge block shows small eastward displacement because of the opposite motions from the rupture on the northern and southern fault segments.

Supplementary Materials

1. **Geodetic observations and three-dimensional co-seismic displacements**

Both Sentinel-1 and ALOS-2 (advanced land observation satellite-2) SAR data

(see Table S1 for details) are used to obtain the co-seismic displacement observations of Maduo earthquake, where the DInSAR (differential interferometric SAR)[*Gabriel et al.*, 1989], POT (pixel offset tracking)[*Michel et al.*, 1999], MAI (multiple aperture interferometry)[*Bechor and Zebker*, 2006], and/or BOI (burst overlap interferometry)[*Grandin et al.*, 2016] methods are employed to process these SAR images based on the GAMMA software. The SRTM (shuttle radar topographic mission) 1-arc-second DEM (digital elevation model) data is used here for correcting the topographic component and for assisting in co-registration process. We apply the multi-look operation of 30×8, 8×20, and 5×32 (range×azimuth) for Sentinel-1, ascending strip-map-mode ALOS-2, and descending ScanSAR-mode ALOS-2 SAR images, respectively, and the final resolution of displacement observations is about 100m×100m. Particularly for the descending ScanSAR-mode ALOS-2 data, there are five separate beams, and each beam is separately processed based on the DInSAR, MAI and POT methods, then mosaiced together in the geographical coordinate system based on the overlaps between adjacent beams.

The DInSAR interferograms are filtered by the adaptive filter based on local fringe spectrum[*Goldstein and Werner*, 1998], and unwrapped by the minimum cost flow method[*C W Chen and Zebker*, 2002]. For the L-band ALOS-2 data, due to its longer wavelength, the corresponding interferograms are contaminated with the ionospheric delays. For the ascending strip-map-mode ALOS-2 SAR images with small coverage, we correct the contained ionospheric delay by first degree polynomials. For the descending ScanSAR-mode ALOS-2 SAR images, we apply a range split spectrum method[*Gomba et al.*, 2016] to mitigate the ionospheric delay[*J Liu et al.*, 2021]. Different from the DInSAR method that can only obtain displacements along the LOS (line-of-sight) direction, the POT method can obtain displacements along both the LOS and azimuth directions. Before the POT process of Sentinel-1 data, the SAR images should be deramped[*Wegmüller et al.*, 2016]. To obtain the pixel offset, we employ a matching window size of 128×128 pixels with the oversampling factor of two for all SAR images, and use a second-order polynomial to fit the possible ramp based on the signals in the far-field regions[*J Hu et al.*, 2012]. Due to the significant ionospheric disturbs, the POT azimuth displacements from the ALOS-2 images can hardly recognize any valuable displacement signals. The signal-to-noise ratio (SNR) of POT displacements is generally proportional to the spatial resolution of SAR images, and may also be affected by the spatial baseline of SAR images from the comparison between the ascending/descending Sentinel-1 POT azimuth displacements. Similar to the POT azimuth observations of ALOS-2 data, the MAI observations are also seriously contaminated by the strip-shape ionospheric disturbs. Due to the limited azimuth doppler bandwidth and spatial resolution, the MAI method is not used for the Sentinel-1 data. For the BOI method, it is only applicable for the Sentinel-1 data in the burst overlap area, whose size is about 86km×1.5km (range×azimuth) accounting for about 7.5% of a burst along the azimuth direction. For a target burst overlap area, four SLC (single look complex) images can be obtained from the two successive bursts of

the primary and secondary SAR images, and the BOI azimuth displacement is derived by double differential operation of these four SLC images. Therefore, sixteen displacement observations can be obtained, among which the azimuth displacement observations from the ALOS-2 data contain serious ionospheric delays and the descending Sentinel-1 POT azimuth observation contains serious decorrelations.

To calculate the three-dimensional (3D) co-seismic displacements, a InSAR-based Strain Model and Variance Component Estimation method (SM-VCE)[*J Liu et al.*, 2018; *J Liu et al.*, 2019a] is used to combine the remaining 11 displacement observations. The strain model represents the geophysical relationship between adjacent points' 3D displacements[*Guglielmino et al.*, 2011], and can be used to establish the observing function between the 3D displacements at a target point and its surrounding observations within a window. Compared with the traditional methods that calculate the 3D displacements of a target point based only on observations on this point[*Jung et al.*, 2011; *Wright et al.*, 2004], the SM-VCE method can incorporate context observations in the calculation. Besides, the relative weight of different observations in the SM-VCE method is determined by the well-known variance component estimation method in a posteriori way[*S W Hu and Xiao*, 2016], which is more accurate than the weight determined by some a priori information about the observation noise.

Since the observations within a window are used to establish the observing function, in the final 3D displacement field, it is possible for the SM-VCE method to fill in some gaps in the observations. Some band-shaped signals are observed in the north-south displacement field, which can be attributed to the fact that the BOI observations are only available in the burst overlap regions and more sensitive to the north-south component than the east-west. In addition, one key point for SM-VCE method is the window size when establishing the observing function based on the strain model. In the window, the displacement gradient is assumed to be constant[*Guglielmino et al.*, 2011]. If the window size is too large, this assumption would be violated, while if too small, there are insufficient data points to suppress the high-frequency noise (e.g., the random noise in the Sentinel-1 POT azimuth observations). In this paper, the window size of 31×31 pixels is empirically determined after comparing with the result of other window sizes. Besides, when calculating 3D displacements for a target point near the fault rupture region, heterogeneous observations at both sides of the fault would be included in the window, which is undesirable and would deteriorate the 3D displacements. In this paper, the fault traces are manually mapped from the ascending Sentinel-1 POT LOS observation, and then used to discard the observations within the window across the fault.

1. **Finite fault inversion**

We derive the FFM with a simulated anealing inversion method [*Ji et al.*, 2002], which allows the joint inversion of seismic waveforms and static deformation data. Since seismic and static data provide complementary constraints on the kinematic rupture process, joint inversion can greatly suppress trade-off among

model parameters.

The seismic waveform dataset includes teleseismic P and SH waves, regional broadband and nearby high-rate GPS waveform records. We download teleseismic waveform data from IRIS (http://www.iris.edu) recorded by the Global Seismological Network (GSN) that has the most uniform spatial coverage to provide best teleseismic (30° - 90°) dataset for FFM inversion. We selected 42 P-waves and 39 SH-waves based on the data quality and azimuthal coverage. Instrument responses are removed from the raw waveform data and converted to displacement after a low-pass filtering with corner frequency of 1.0 Hz. Although 1Hz is relatively high frequency for deterministic inversion, the waveforms are dominated by relatively low frequency energy. We also use three-component 1Hz high-rate GPS waveform observaations recorded by 10 nearest stations (Fig.S4), see *Gao et al.* [2021] for the detailed GPS data processing and data availability. The sampling rate of the GPS data is 1 Hz, so in the inversion we filter these data to 0.02 to 0.4 Hz. Besides, three-component displacement waveform records of 7 regional broadband stations are also included in the inversion (top traces in Fig.S3). These broadband stations are part of the national broadband seismic network. Both the regional and teleseismic Green's functions are calcualted with a Tibet crustal velocity model proposed by *L Zhu and Helmberger* [1996] using a frequency-wavenumber integration method[*L P Zhu and Rivera*, 2002].

We use 6 down-sampled InSAR and SAR datasets in the joint inversion. We did not inlcude all the datasets in Fig.S1 in the inversion, only the images that have high data quality are used. For InSAR data, we solve for quadratic ramps in the inversion to correct for orbital errors. The static green's functions at free surface are calculated by using the same 1D velocity model[*L Zhu and Helmberger*, 1996] as for the dynamic Green's function.

To parameterize the finite fault model, we divide the rectangle fault plane into smaller sub-faults and solve for the slip amplitude and direction, risetime and rupture velocity on each sub-fault. For each parameter, we specify the bounds and a discretization interval. The bounds and increments are selected based on trial-and-error. We define the misfit function as:

$$E_{wf} + W_I \times E_I + W_S \times S + W_M \times M$$

where E_{wf} is the waveform misfit. E_I is the geodetic misfit, S is a normalized, second derivative of slip between adjacent patches (smoothing), M is a normalized seismic moment, and W_I, W_S and W_M are the relative weighting for the geodic misfit, smoothing, and seismic moment, respectively. In the joint inversion, the relative weighting is realized by normalizing the misfit of each dataset by the misfit derived by inverting the individual dataset. Based on our previous experiences (e.g. [*Wei et al.*, 2011]) we set the weight for the geodetic misfits double that of the waveform misfits. A simulated annealing algorithm[*Ji et al.*, 2002] is adopted to find the best fitting model parameters in the joint.

We set the sub-fault size to be 3 km × 2 km, constrain the rake angles to be

between -45° to 45°, and allow rupture velocity to vary between 3.0- 2.0 km/s, as guided by the back-projection results. We also assume the risetime to be an arc of the cosine function and to vary between 1.0 and 9.0 s with 0.8 s steps. The slip amplitude can change from 0 to 6 m. Note that the selection of rupture speed range is narrowed down by the BP results, which can reduce the trade-offs between rupture speed and risetime.

We use 10 fault segments (Table S2) to mimic the primary variations of strike as revealed in the 3D deformation (Fig.S2). The dip direction and dip angle of these fault segments are determined by fitting the geodetic observations and the aftershock distribution. We then conduct joint inversion of waveform data and the geodetic data. Our preferred finite fault model is presented in Fig.2a and Fig.3, with the waveform fittings presented in Fig.S3-5 and the geodetic data fitting shown in Fig.S6-8. As shown in these figures, both datasets are very well fitted. To further verify the quality of waveform fitting, we also convert the horizontal components of the high-rate GPS waveform to velocity and filter them to 0.02 to 0.4 Hz, which still show good agreements between data and the synthetics (Fig.S4a). At broadband, both the dynamic waveforms and the static offsets in these GPS data are also well-fitted (Fig.S4b).

1. **Multiple Point Source Inversion**

To constrain the first order complexity of the rupture process of the Maduo mainshock, we conduct a multiple point source (MPS) inversion[*Q Shi et al.*, 2018] using nearby high-rate GPS waveforms, regional broadband waveforms and teleseismic body waves. The same high-rate GPS data used in the FFM inversion are adopted here. We download the teleseismic broadband data from the Incorporated Research Institutions for Seismology (IRIS) data centre and regional broadband data (within the epicentre distance of 800 km) from China Earthquake Networks Centre (CENC). We remove the instrument response for the downloaded data and select 61 regional broadband stations and 49 teleseismic stations with relatively even azimuthal coverage based on their coordinates (Fig. S9) and data quality (e.g., signal to noise ratio, whether the waveform is clipped).

We conduct MPS inversion using the Markov Chain Monte Carlo (MCMC) sampling algorithm that is proposed by [*Q Shi et al.*, 2018]. Considering the different site condition and 3D velocity structure, we apply station-dependent filtering to the regional and teleseismic waveforms. At the same time, we apply broader band for the high-rate GPS waveforms. The determination of frequency ranges is initially based on the similar degree of complexities of the observations and synthetics. We then conduct the MPS inversion in an iterative fashion and further refine the frequency ranges with updated MPS solutions. We start the inversion using three point-sources, and then gradually increase to seven sources. Here, we show the optimal waveform fitting is achieved using six point-sources.

The rupture process of the Mw7.4 earthquake is well represented by six point-sources (Figure 2 and Figure S10-12). The statistics of waveform

cross-correlation coefficients are shown in Figure S13. The first subevent (Mw7.07) is located near the epicentre of the earthquake, only about 7 km to the southeast. The following subevents show a bilateral rupture processes, with two subevents (Mw6.95 and Mw6.55) located to the west and the other three (Mw6.93, Mw6.84 and Mw6.83) located to the east of the first subevent. We add together the moment-weighted moment tensor of the six subevents to calculate the cumulative moment tensor, which shows a relative small compensated linear vector dipole (CLVD) component. It should be noted that the CLVD percentage in the cumulative moment tensor is mainly contributed by the oblique north-dipping subevent that is located near the west end of the fault.

1. **Back-projection**

We back-project teleseismic high frequency waveform data recorded by the Australian (AU) and European (EU) arrays (Fig. S14) to image the rupture process of the Maduo earthquake. Traditionally, beginning portion of the array P-waves is align to calibrate the 3D velocity structure and this calibration is applied to the rest of the rupture area. However, due to 3D velocity structure at the source side, the calibration obtained for the beginning portion may not be sufficient for later part of the rupture that are located further away from the epicenter. To handle this issue and improve the BP resolution, we apply a new travel-time calibration strategy [*Zeng et al.*, 2022] to the MUltiple SIgnal Classification BP method[*Meng et al.*, 2011; *Zeng et al.*, 2020] to better resolve the high-frequency (HF) radiation of the 2021 Mw 7.4 Maduo earthquake. To understand the performance of the new calibration and derive an uncertainty estimation, we use the conventional calibration and the new calibration strategy to relocate M>5 earthquakes, mostly aftershocks, that are located near the surface rupture. The BP locations of these events are then compared with the relocation results from [*W Wang et al.*, 2021] (Fig. S15). We first note that in both conventional and calibrated BP relocation results, events located to the west/east of the mainshock hypocenter have large mis-relocation in AU/EU arrays, respectively. Considering that in the calibrated BP we assume velocity heterogeneities bias travel-time error linearly, this mis-relocation pattern change around the mainshock epicenter may indicate some structural heterogeneities here. Compared with relocation from conventional BP, relocation from the calibrated BP using EU data can better match the catalog location in west of the epicenter. Relocation from the calibrated BP using AU data has similar resolution as conventional BP. Considering the different mis-location pattern we observed, therefore, to reach higher resolution, we use AU and EU arrays to image the east and west propagation ruptures, respectively. And the average mis-location results in a lower bound uncertainty estimation of 7.5 and 4.5 km for calibrated BP using AU and EU array data.

Supplementary Tables and Figures

Table S1. The detailed information of the SAR data used in this paper

Sensor	Orbit direction	Master and slave date	Spatial perpendicular baseline (m)	Wavelength (cm)	Incident angle (deg.)	Azimuth angle (deg.)	Pixel resolution (m) (range × azimuth)	Imaging mode
Sentinel-1	Asc	May 2021 26 May 2021					×13.98	TOPS
Sentinel-1	Des	May 2021 26 May 2021					×13.98	TOPS
ALOS-2	Asc	May 2020 24 May 2021					×3.78	Strip-map
ALOS-2	Des	Dec. 2020 4 Jun. 2021					×2.60	ScanSAR

Table S2 strike and dip angles of the 10 fault segments used in finite fault inversion.

No. Seg	1	2	3	4	5	6	7	8	9	10
Strike(°)	275	288	284	293	268	285	96	82	115	93
Dip(°)	75	80	70	70	80	80	80	80	80	80

Table S3 Multiple-Point-Source solution for the Maduo Earthquake

event No.	Lon.(°)	Lat. (°)	Dep. (km)	Strike (°)	Dip (°)	Rake (°)	Mw	Centroid Time (s)
M1	97.6642	34.7567	3.37	268	56	-43	6.55	26.8
M2	97.9043	34.7198	6.10	278	67	-3	6.95	21.7
M3	98.4944	34.6256	7.81	290	88	-1	7.07	7.3
M4	98.7055	34.5250	7.82	283	81	3	6.92	14.0

event No.	Lon.(°)	Lat. (°)	Dep. (km)	Strike (°)	Dip (°)	Rake (°)	Mw	Centroid Time (s)
M5	99.0050	34.5197	5.26	106	89	2	6.84	21.9
M6	99.0494	34.4505	4.48	282	89	0	6.83	24.8

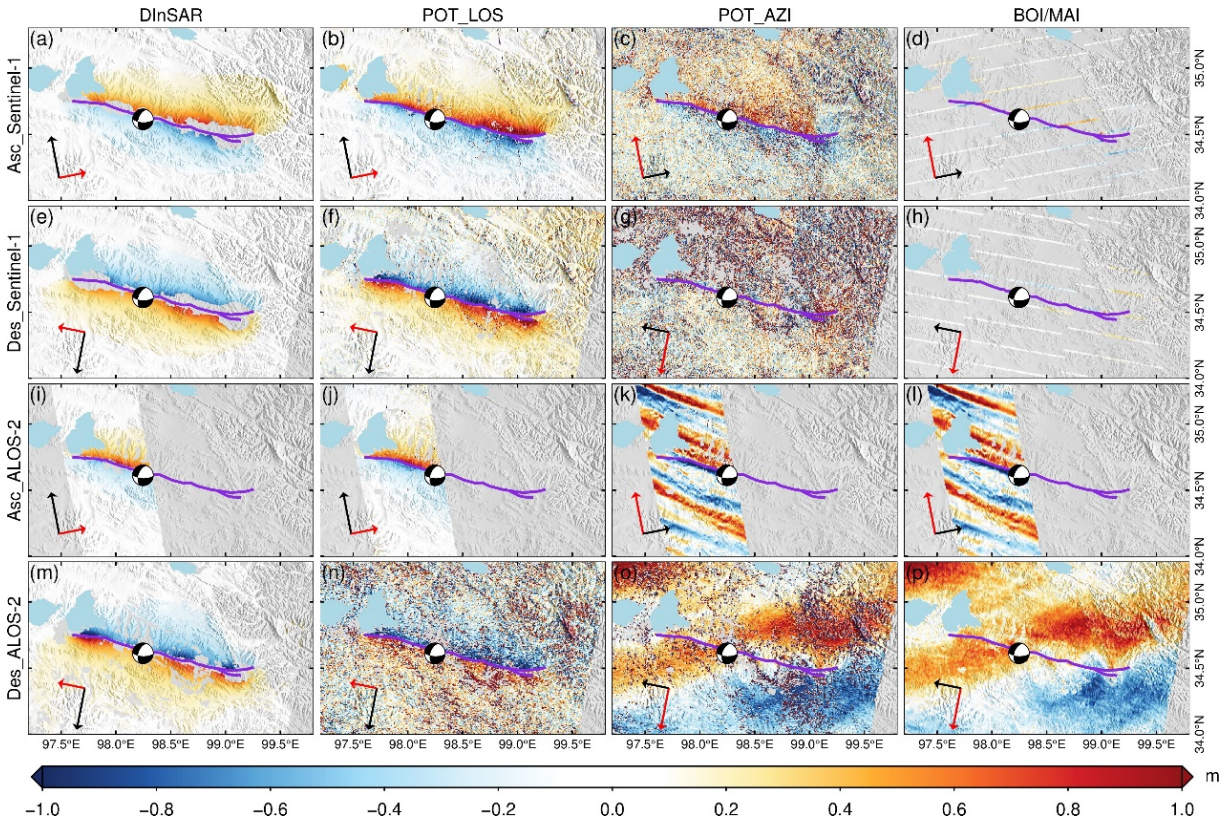

Figure S1. Displacement observations along the LOS and azimuth directions from ascending/descending (Asc/Des) Sentinel-1/ALOS-2 SAR data based on the DInSAR, POT, MAI, and/or BOI methods. Longer and shorter arrows represent the azimuth and LOS directions, respectively, the red arrow corresponds to the observing direction of each observation. The purple lines show the location of ruptured fault traces.

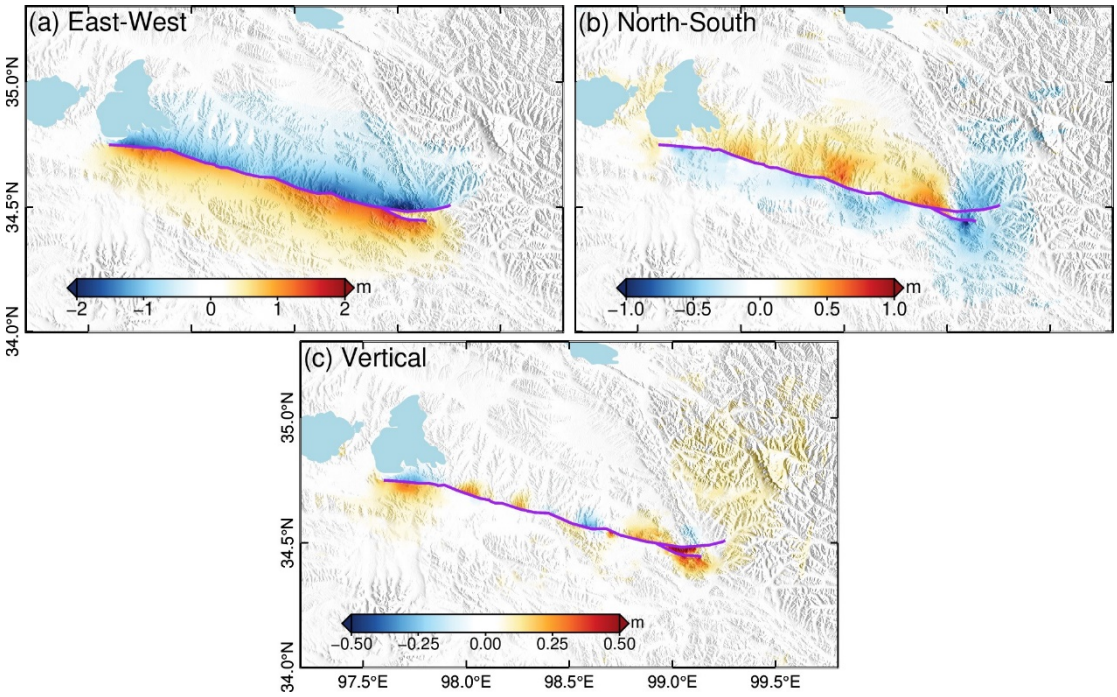

Figure S2. 3D co-seismic displacements of the 2021 Maduo earthquake calculated by the SM-VCE method.

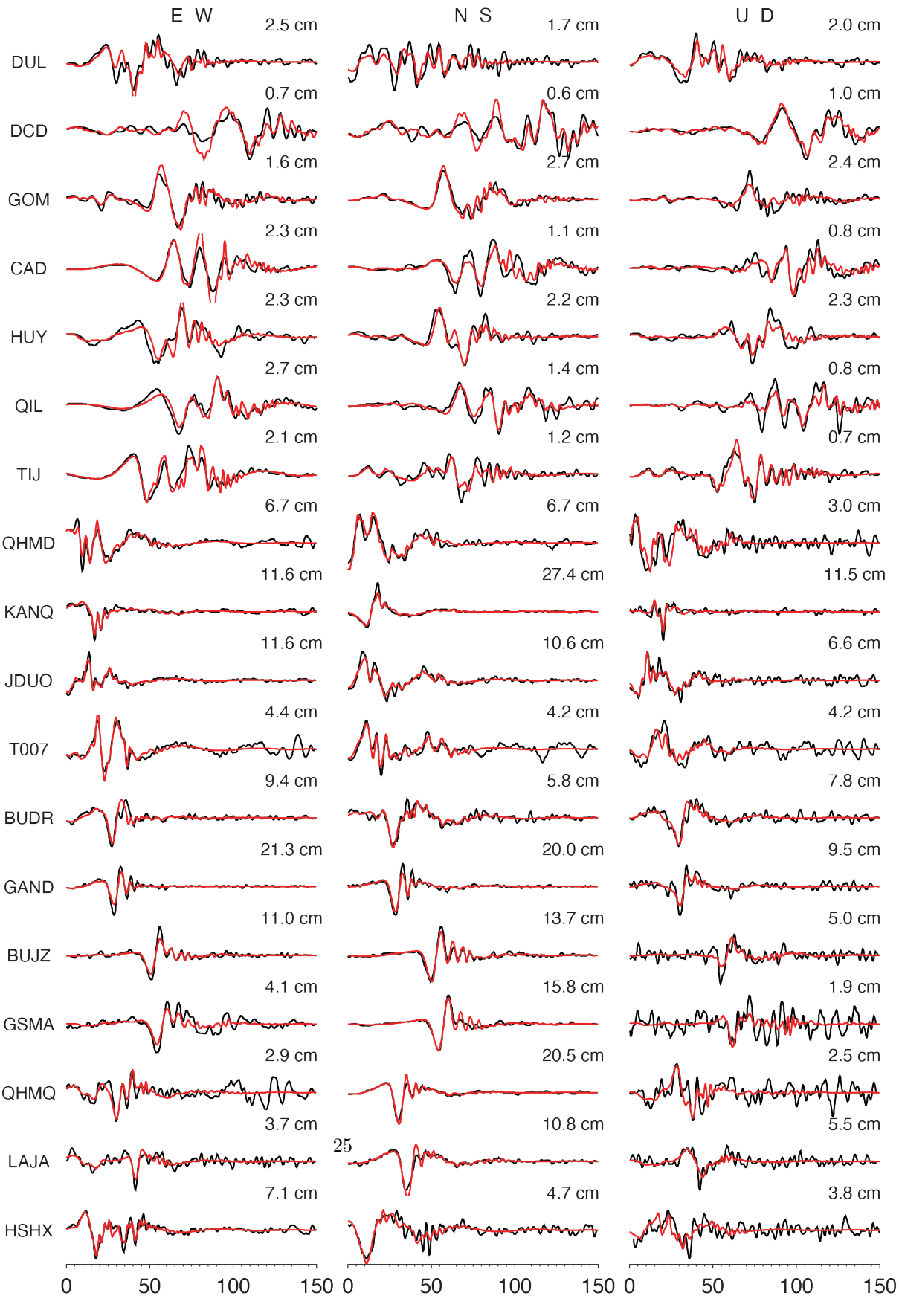
E W
N S
U D
DUL
DCD
GOM
CAD
HUY
QIL
TIJ
QHMD
KANQ
JDUO
T007
BUDR
GAND
BUJZ
GSMA
QHMQ
LAJA
HSHX
2.5 cm
0.7 cm
1.6 cm
2.3 cm
2.3 cm
2.7 cm
2.1 cm
6.7 cm
11.6 cm
11.6 cm
4.4 cm
9.4 cm
21.3 cm
11.0 cm
4.1 cm
2.9 cm
3.7 cm
7.1 cm
1.7 cm
0.6 cm
2.7 cm
1.1 cm
2.2 cm
1.4 cm
1.2 cm
6.7 cm
27.4 cm
10.6 cm
4.2 cm
5.8 cm
20.0 cm
13.7 cm
15.8 cm
20.5 cm
10.8 cm
4.7 cm
2.0 cm
1.0 cm
2.4 cm
0.8 cm
2.3 cm
0.8 cm
0.7 cm
3.0 cm
11.5 cm
6.6 cm
4.2 cm
7.8 cm
9.5 cm
5.0 cm
1.9 cm
2.5 cm
5.5 cm
3.8 cm
0
50
100
150
time(s)
25

Figure S3. Displacement waveform fits between high-rate GPS, broadband regional observations (black) and the synthetics (red). Both data and synthetics are filtered to 0.02 – 0.4 Hz. The largest amplitude in the data for each component is shown at the end of each waveform pair.

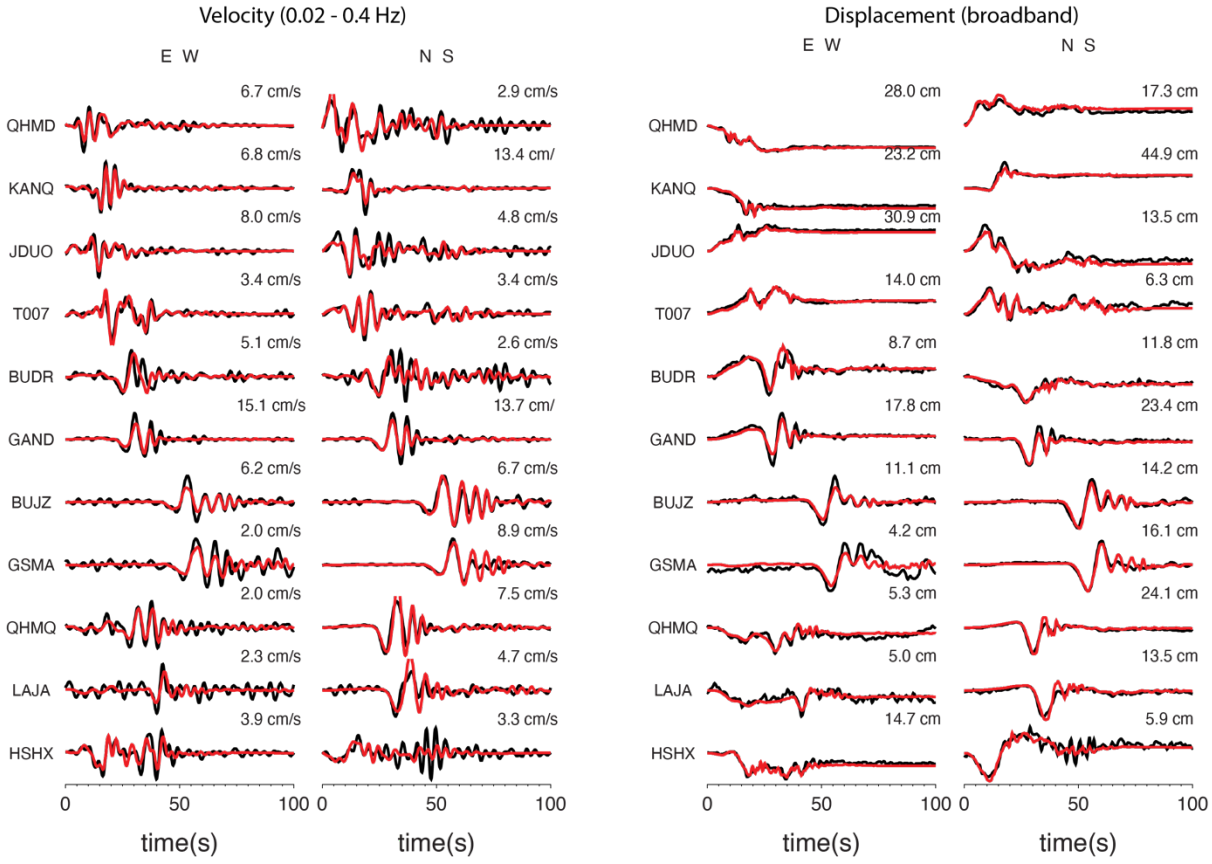

Figure S4. Velocity and broadband displacement waveform comparison between data and the synthetics.

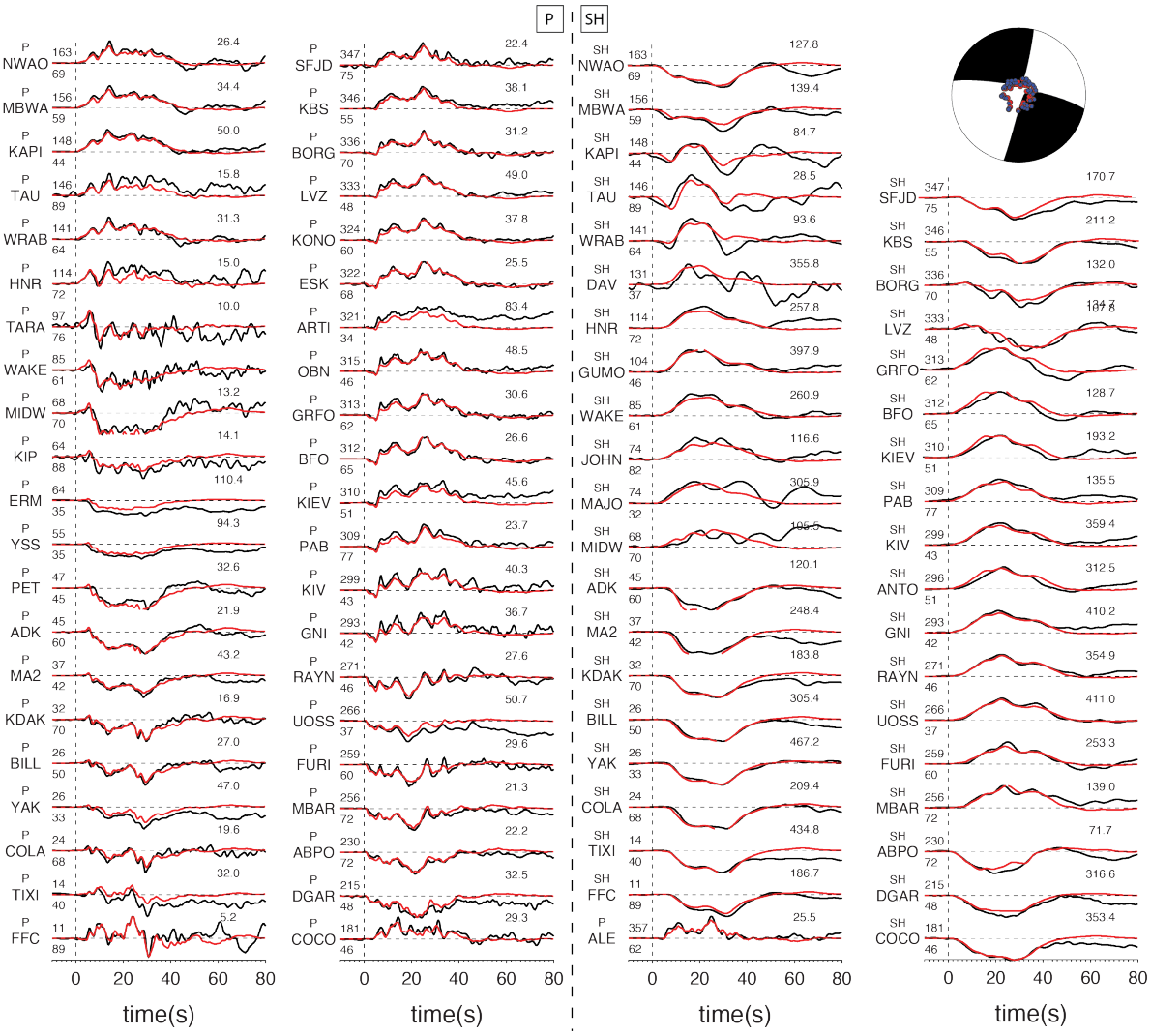

Figure S5. Teleseismic waveform fits for P (vertical) and SH waves. Both data (black) and synthetics are in displacement, with the maximum amplitude of data in micro-meter indicated at the end of each waveform pair. Station ID and component name are indicated at the beginning of each trace, next to the epicenter distance (lower) and azimuth (upper) in degree. The beach ball represents the equivalent moment tensor from finite fault model, with the projection of P-wave stations shown as blue circles and SH-wave stations shown as red circles.

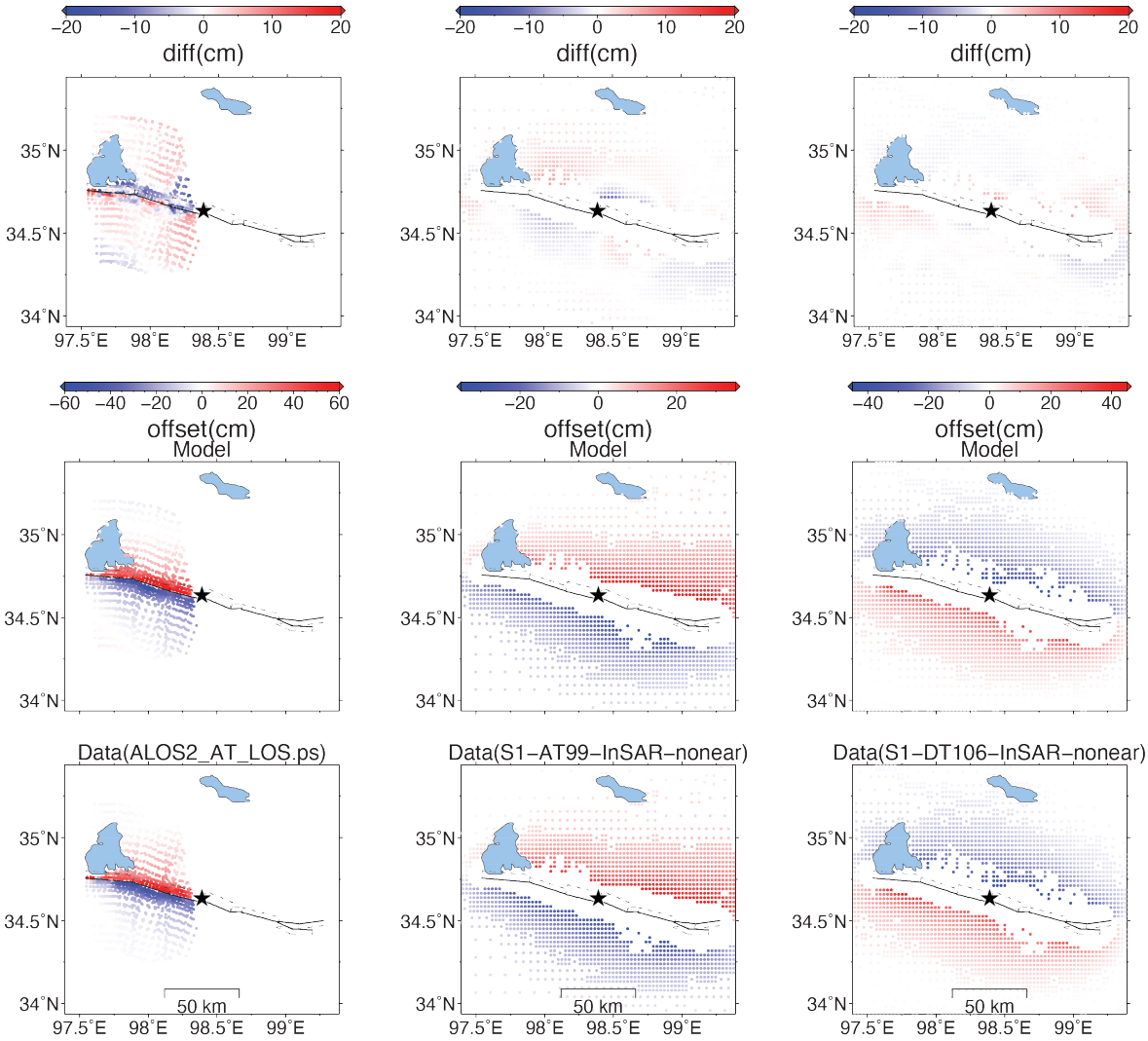

Figure S6. Data fits from the joint inversion for three InSAR interferograms. The data is shown at the bottom row with track names indicated at the top of each panel. The middle row shows the synthetics and the differences between data and synthetics are presented at the top row.

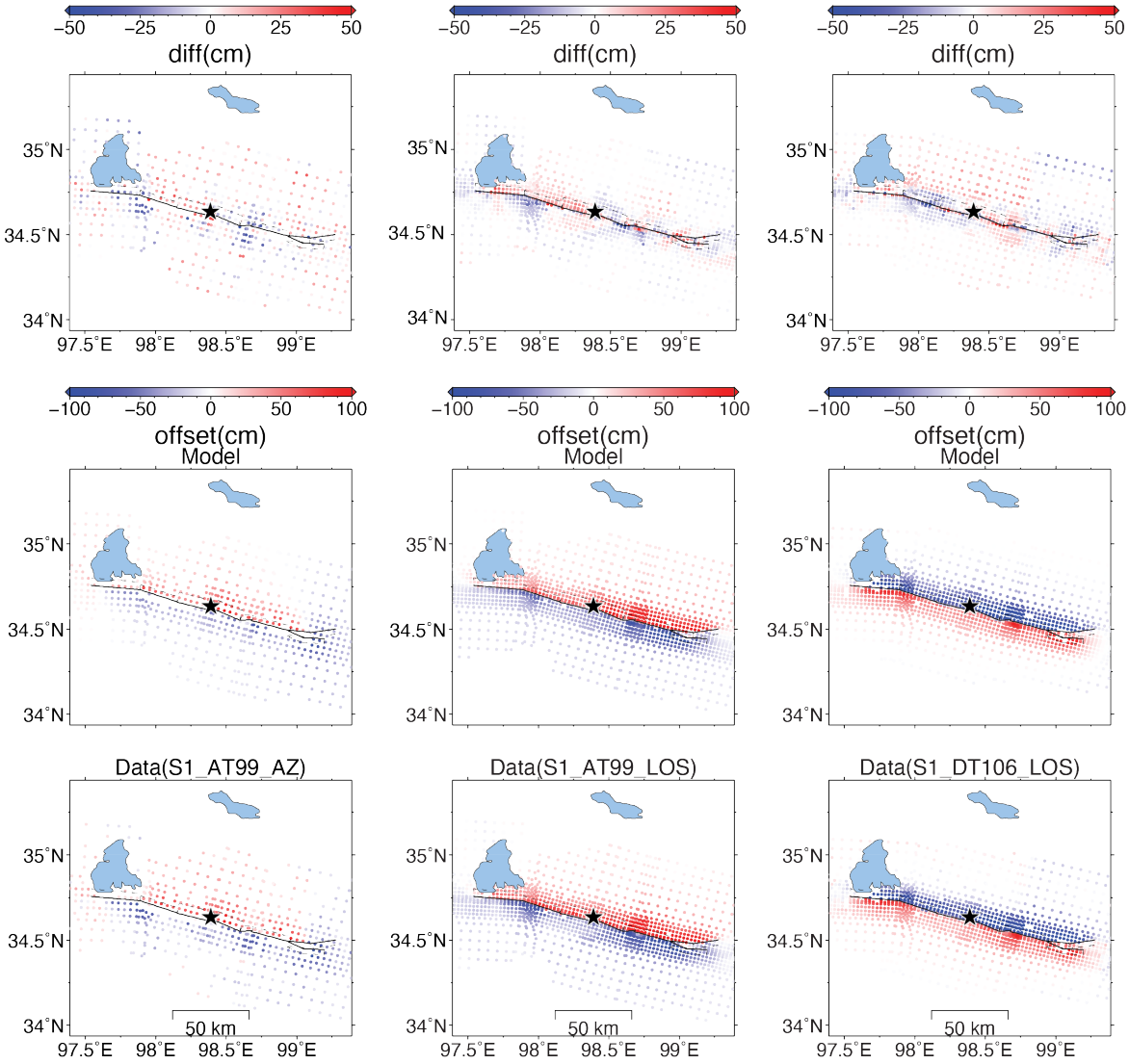

Figure S7. Data fits from the joint inversion for three SAR images. The data is shown at the bottom row with track names indicated at the top of each panel. The middle row shows the synthetics and the differences between data and synthetics are presented at the top row.

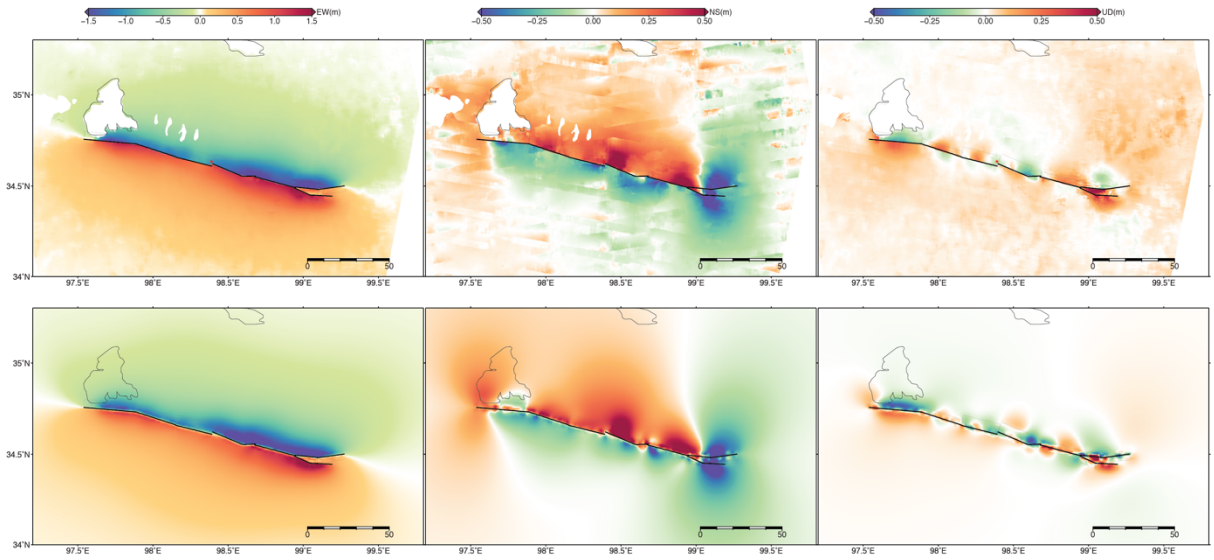

Figure S8. 3D surface deformation and comparison with the prediction from the preferred model. The synthetics are shown in the lower panels and the observations are shown in the upper panels. Fault segments used in the finite fault model are indicated by the rectangles and the red stars represent the epicenter.

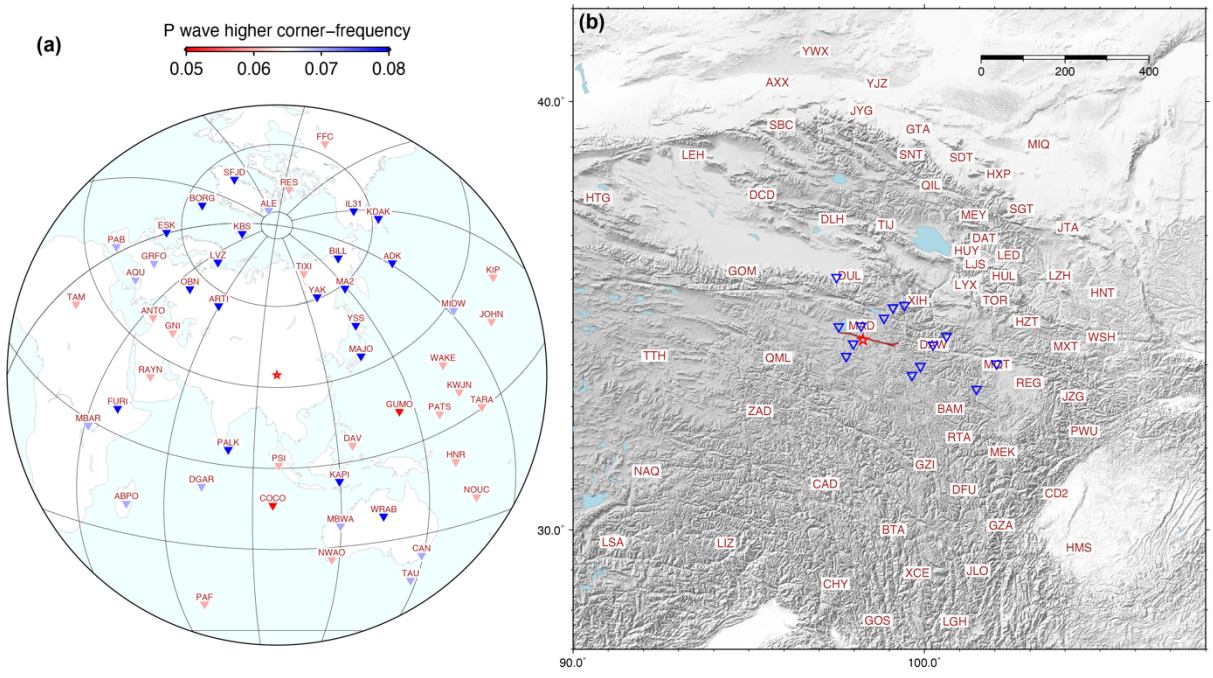

Figure S9. (a) Teleseismic station distribution used in MPS inversion, colored by the higher corner frequency used to filter the P-waves. (b) Regional broadband stations (red text) and high-rate GPS stations (blue triangles) that are used in the MPS inversion. Red star indicates the epicenter and the red line indicates the fault trace of the 2021 Mw7.4 Maduo earthquake.

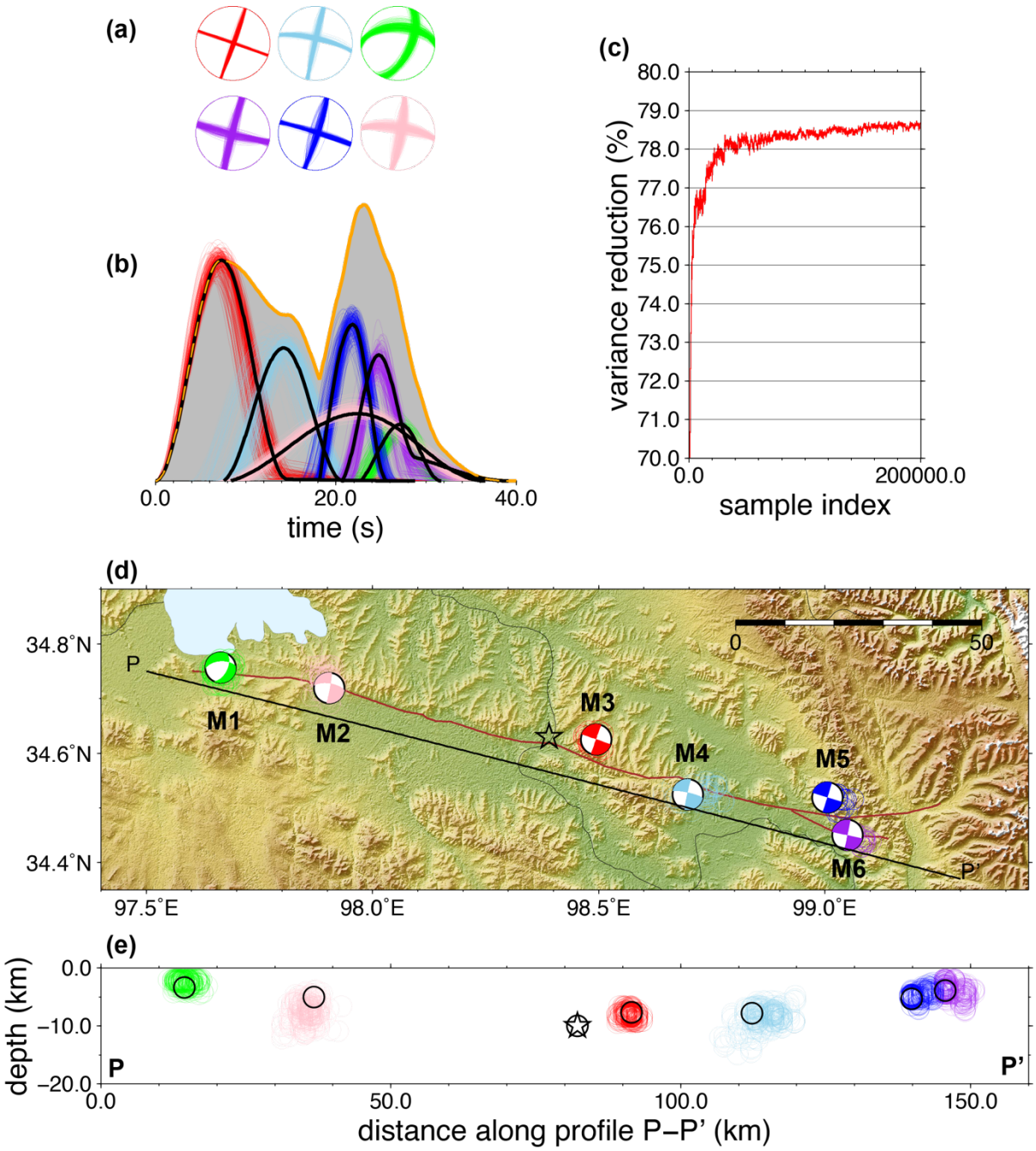

Figure S10, Preferred MPS solution of the 2021 Mw7.4 Maduo earthquake that composes of 6 sub-events. (a) Double-couple solution of each sub-event, multiple lines in the beach balls represent the last 100, 000 samples in the inversion. The

color of each sub-event is corresponding to that in (b), (d) and (e). (b) Source time function of each sub-events. The total source time function is indicated by the orange line. (c) Variance reduction shown as a function of number of iterations in the MCMC inversion. (d) Map view of the subevents, the locations of the last 100,000 iterations are also shown as circles. Epicenter is shown as the star and the red lines represent the surface rupture traces derived from the geodetic data (e) Depth view of the solution along the P-P' profile.

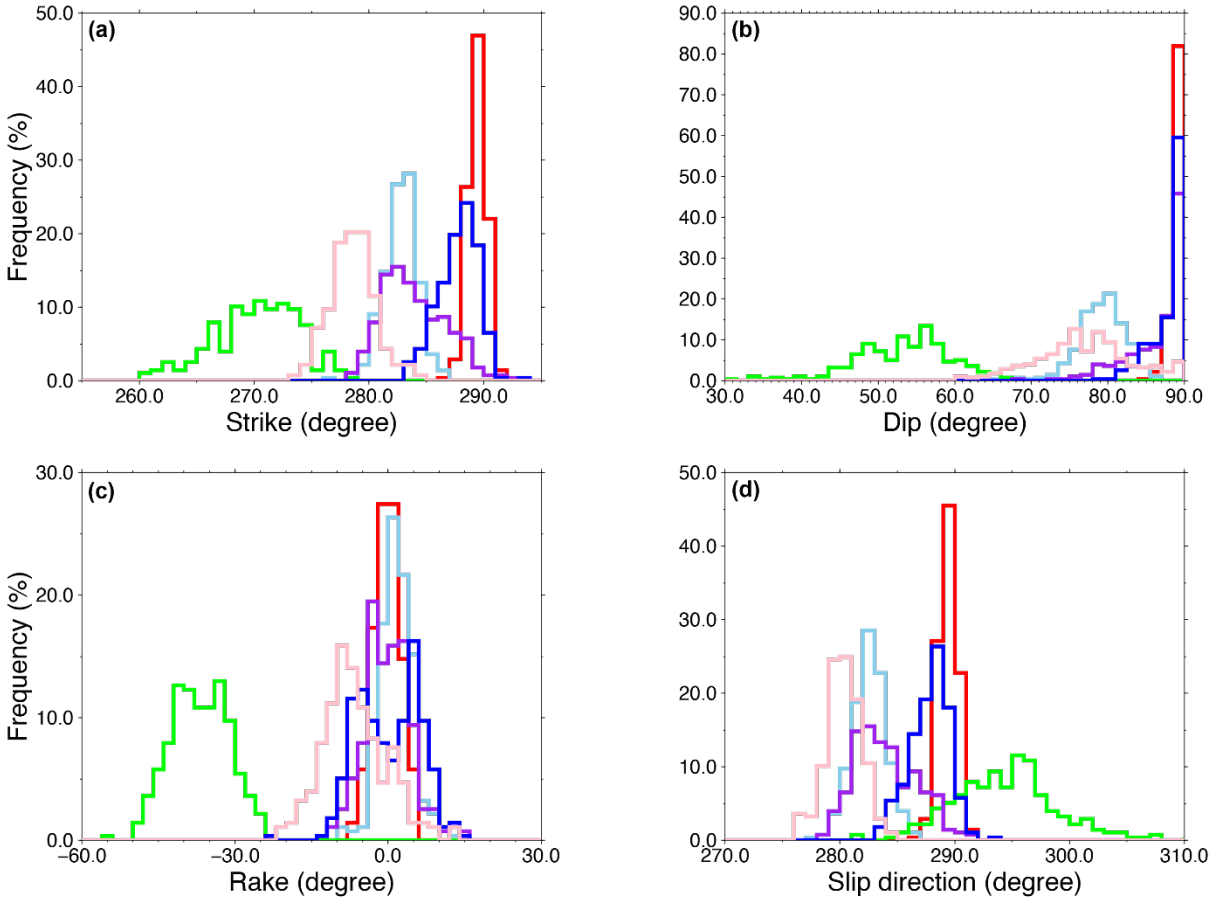

Figure S11. MCMC samples of strike (a), dip (b), rake (c) and north-wall horizontal slip direction (d) of the six sub-events of the MPS solution in the last 100,000 iterations. See Fig.S9 for the color and location of each subevent.

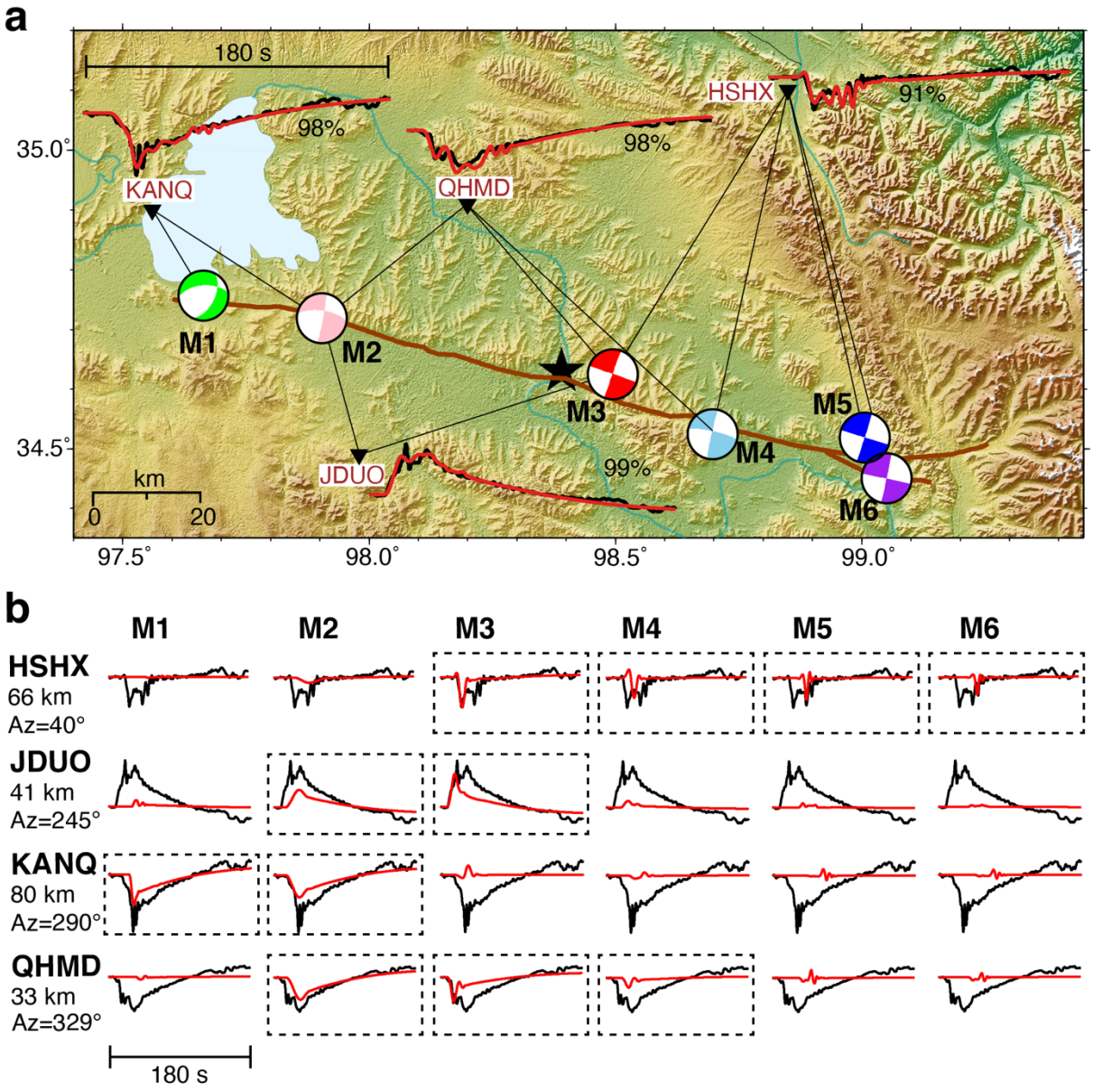

Figure S12. Sub-event sensitivities and E-W component waveform decompositions of the nearby four high-GPS stations. (a) Map view of the six sub-events and high-rate GPS waveform fitting where filtered data is shown in black, synthetics are shown in red and cross-correlations coefficients (CC) are indicated alongside. Each GPS station is mostly sensitive to the subevents connected with straight lines to the station. (b) Decomposed sub-event synthetics (red waveforms of each column) show dominant contributions to different GPS sta-

tions and represent their strong necessity in explaining the data (black). Station name, epicenter distance and azimuths are listed on the left.

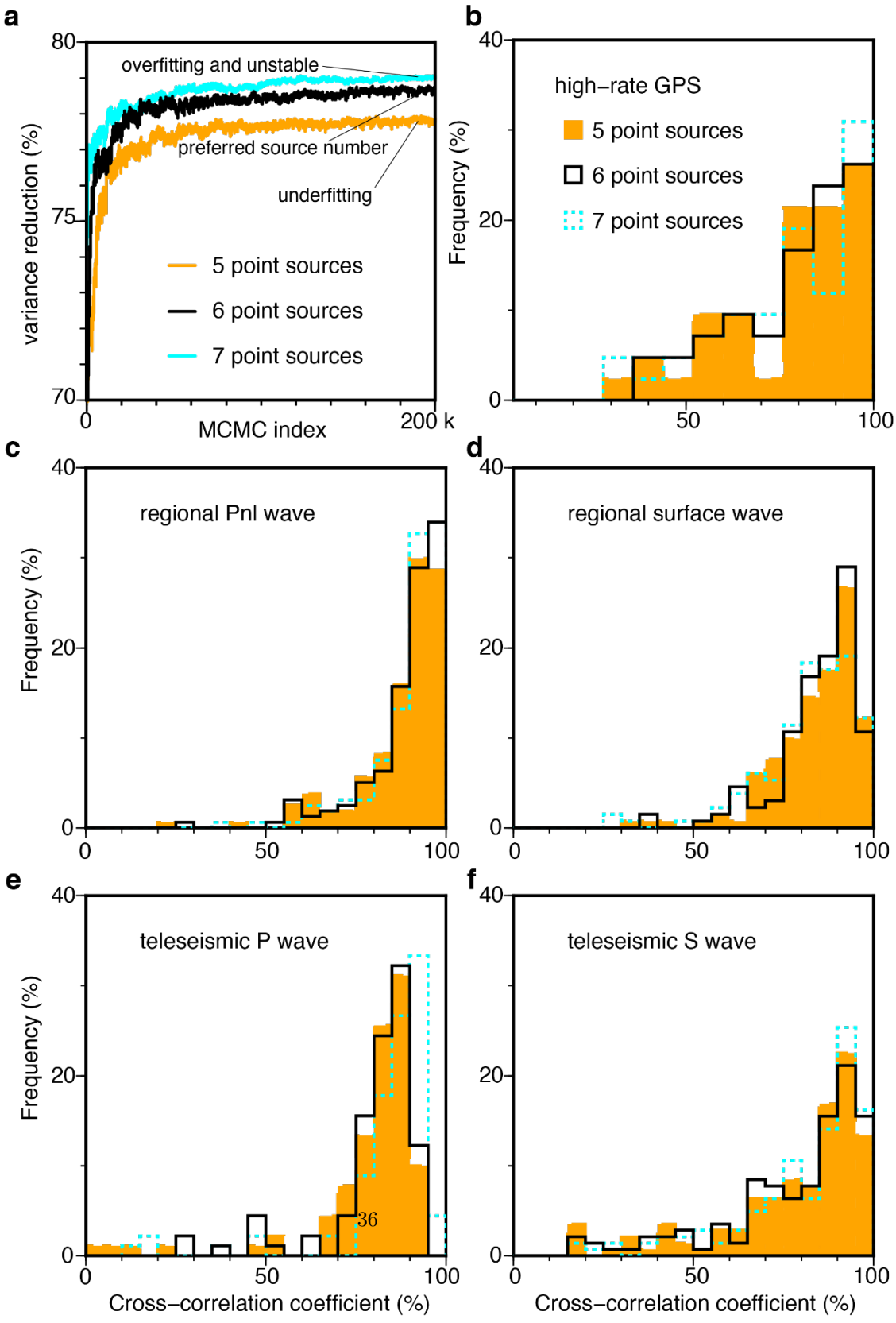
a
80
75
70
overfitting and unstable
preferred source number
underfitting
variance reduction (%)
5 point sources
6 point sources
7 point sources
0
MCMC index
200 k
b
40
20
0
high−rate GPS
5 point sources
6 point sources
7 point sources
Frequency (%)
50
100
c
regional Pnl wave
Frequency (%)
d
regional surface wave
e
teleseismic P wave
Frequency (%)
Cross−correlation coefficient (%)
f
teleseismic S wave
Cross−correlation coefficient (%)

Figure S13. Quality of MPS data fitting and comparison on the total number of MPS sub-events. (a) The variance reduction is being improved during the MCMC inversion processes of 5-, 6- and 7-sub-events, before it reaches a 'plateau'. The optimization efficiency is greatly improved by using 6-sub-events compared to 5-sub-events, but the improvement is less evident when using 7-subevents. (b)-(f) Statistics of cross-correlation coefficients of high-rate GPS, regional Pnl, regional surface wave, teleseismic P and teleseismic S wave components shows systematic improvement of using 6-sub-events compared to 5-subevents. 7-sub-events shows better fits to teleseismic data but poorer fits to local GPS and regional waveform observations.

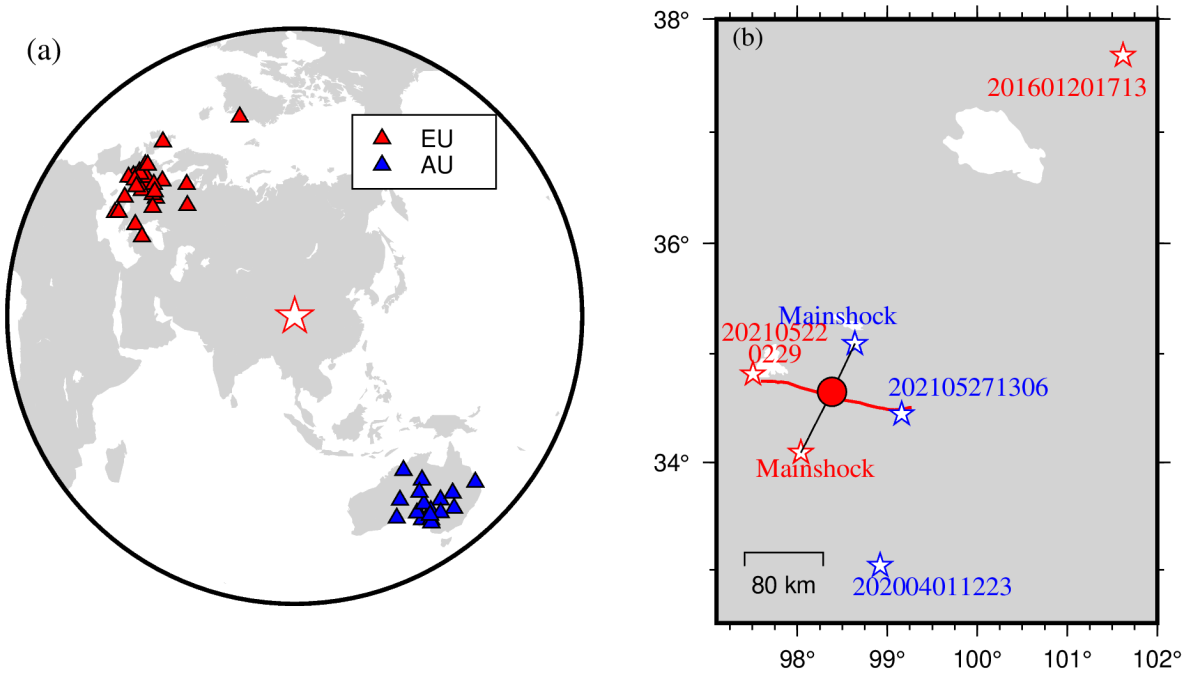

Figure S14. (a) Distribution of used stations in BP. Blue and red triangles are stations in AU and EU arrays. (b-d) Used calibration events for conducting BP in AU (red stars) and EU (blue stars) arrays. The 201601201713 and 202004011223 events are a little bit far away from the main-shock rupture area, so they are presented in different sub-figures.

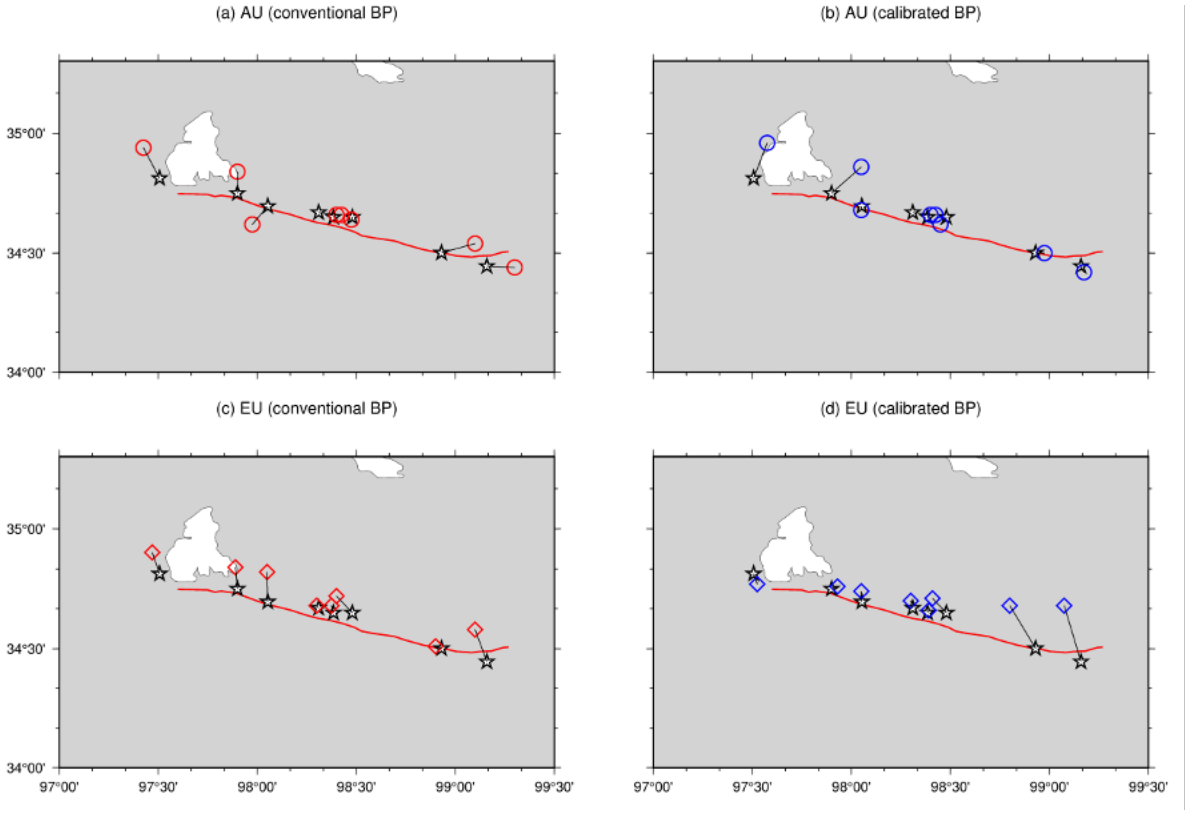

Figure S15. Relocation of near fault events (M>5) using the conventional BP (a-AU, c-EU) and the new calibrated BP (b-AU, d-EU). White stars are events in the source region with magnitude>5 from [*W Wang et al.*, 2021].

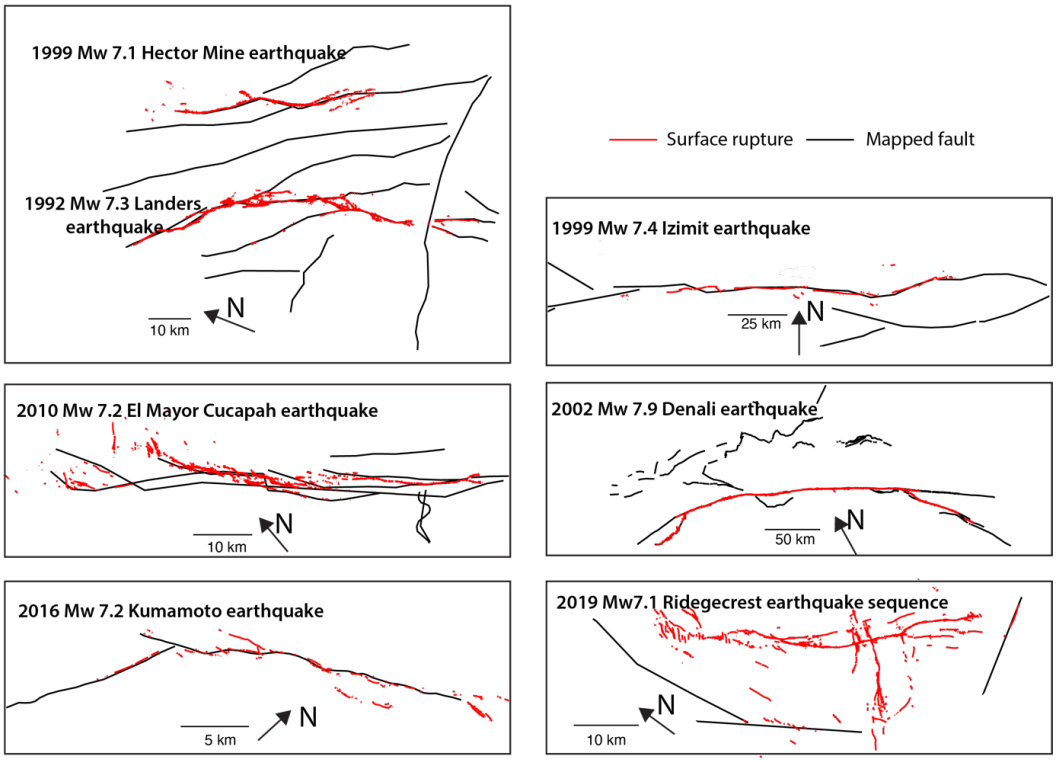

Figure S16. Surface rupture of several well-recorded strike-slip earthquakes in the past few decades [*Baize et al.*, 2020].

References:

Aochi, H., and E. Fukuyama (2002), Three-dimensional nonplanar simulation of the 1992 Landers earthquake, *Journal of Geophysical Research: Solid Earth*, *107*(B2), ESE 4-1-ESE 4-12.Aochi, H., R. Madariaga, and E. Fukuyama (2002), Effect of normal stress during rupture propagation along nonplanar faults, *Journal of Geophysical Research: Solid Earth*, *107*(B2), ESE 5-1-ESE 5-10.Baize, S., F. Nurminen, A. Sarmiento, T. Dawson, M. Takao, O. Scotti, T. Azuma, P. Boncio, J. Champenois, and F. R. Cinti (2020), A worldwide and unified database of surface ruptures (SURE) for fault displacement hazard analyses, *Seismol Res Lett*, *91*(1), 499-520.Bechor, N. B. D., and H. A. Zebker (2006), Measuring two-dimensional movements using a single InSAR pair, *Geophys. Res. Lett.*, *33*(16), 275-303, doi:10.1029/2006gl026883.Chen, C. W., and H. A. Zebker (2002), Phase unwrapping for large SAR interferograms: Statistical segmentation and generalized network models, *IEEE Trans. Geosci. Re-*

mote Sens., *40*(8), 1709-1719, doi:10.1109/TGRS.2002.802453.Chen, K., J. P. Avouac, J. Geng, C. Liang, Z. Zhang, Z. Li, and S. Zhang (2022), The 2021 Mw 7.4 Madoi earthquake: an archetype bilateral slip-pulse rupture arrested at a splay fault, *Geophys Res Lett*, e2021GL095243.Douilly, R., D. D. Oglesby, M. L. Cooke, and J. L. Hatch (2020), Dynamic models of earthquake rupture along branch faults of the eastern San Gorgonio Pass region in California using complex fault structure, *Geosphere*, *16*(2), 474-489.Duan, B., and D. D. Oglesby (2007), Nonuniform prestress from prior earthquakes and the effect on dynamics of branched fault systems, *Journal of Geophysical Research: Solid Earth*, *112*(B5).Duputel, Z., H. Kanamori, V. C. Tsai, L. Rivera, L. Meng, J.-P. Ampuero, and J. M. Stock (2012), The 2012 Sumatra great earthquake sequence, *Earth Planet Sc Lett*, *351*, 247-257.Gabriel, A. K., R. M. Goldstein, and H. A. Zebker (1989), Mapping small elevation changes over large areas: Differential radar interferometry, *J. Geophys. Res. Solid Earth*, *94*(B7), 9183-9191, doi:10.1029/JB094iB07p09183.Gao, Z., Y. Li, X. Shan, and C. Zhu (2021), Earthquake Magnitude Estimation from High-Rate GNSS Data: A Case Study of the 2021 Mw 7.3 Maduo Earthquake, *Remote Sens-Basel*, *13*(21), 4478.Goldstein, R. M., and C. L. Werner (1998), Radar interferogram filtering for geophysical applications, *Geophys. Res. Lett.*, *25*(21), 4035-4038.Gomba, G., A. Parizzi, F. D. Zan, M. Eineder, and R. Bamler (2016), Toward Operational Compensation of Ionospheric Effects in SAR Interferograms: The Split-Spectrum Method, *IEEE Trans. Geosci. Remote Sens.*, *54*(3), 1446-1461, doi:10.1109/Tgrs.2015.2481079.Grandin, R., E. Klein, M. Métois, and C. Vigny (2016), 3D displacement field of the 2015 M w 8.3 Illapel earthquake (Chile) from across- and along-track Sentinel-1 TOPS interferometry, *Geophys. Res. Lett.*, *43*(6), 2552-2561, doi:10.1002/2016GL067954.Guglielmino, F., G. Nunnari, G. Puglisi, and A. Spata (2011), Simultaneous and Integrated Strain Tensor Estimation From Geodetic and Satellite Deformation Measurements to Obtain Three-Dimensional Displacement Maps, *IEEE Trans. Geosci. Remote Sens.*, *49*(6), 1815-1826, doi:10.1109/TGRS.2010.2103078.He, K., Y. Wen, C. Xu, and Y. Zhao (2022), Fault Geometry and Slip Distribution of the 2021 M w 7.4 Maduo, China, Earthquake Inferred from InSAR Measurements and Relocated Aftershocks, *Seismological Society of America*, *93*(1), 8-20.Hu, J., Z. Li, J. Zhu, L. Zhang, and Q. Sun (2012), 3D coseismic Displacement of 2010 Darfield, New Zealand earthquake estimated from multi-aperture InSAR and D-InSAR measurements, *J. Geod.*, *86*(11), 1029-1041, doi:10.1007/s00190-012-0563-6.Hu, S. W., and B. L. Xiao (2016), *Modern theory and application of surveying data processing (in Chinese)*, Surveying and Mapping Press, Beijing, China.Ji, C., D. V. Helmberger, D. J. Wald, and K. F. Ma (2003), Slip history and dynamic implications of the 1999 Chi-Chi, Taiwan, earthquake, *J Geophys Res-Sol Ea*, *108*(B9), doi:Artn 2412Doi 10.1029/2002jb001764.Ji, C., D. J. Wald, and D. V. Helmberger (2002), Source description of the 1999 Hector Mine, California, earthquake, part I: Wavelet domain inversion theory and resolution analysis, *B Seismol Soc Am*, *92*(4), 1192-1207, doi:Doi 10.1785/0120000916.Jin, Z., and Y. Fialko (2021), Coseismic and early postseismic deformation due to the 2021 M7. 4 Maduo (China) earthquake, *Geophys Res Lett*, *48*(21), e2021GL095213.Jung,

H. S., Z. Lu, J. S. Won, M. P. Poland, and A. Miklius (2011), Mapping Three-Dimensional Surface Deformation by Combining Multiple-Aperture Interferometry and Conventional Interferometry: Application to the June 2007 Eruption of Kilauea Volcano, Hawaii, *IEEE Geosci. Remote Sens. Lett.*, *8*(1), 34-38, doi:10.1109/LGRS.2010.2051793.Kame, N., J. R. Rice, and R. Dmowska (2003), Effects of prestress state and rupture velocity on dynamic fault branching, *Journal of Geophysical Research: Solid Earth*, *108*(B5).King, G., and J. Nábělek (1985), Role of fault bends in the initiation and termination of earthquake rupture, *Science*, *228*(4702), 984-987.Klinger, Y. (2010), Relation between continental strike-slip earthquake segmentation and thickness of the crust, *Journal of Geophysical Research: Solid Earth*, *115*(B7).Leonard, M. (2010), Earthquake fault scaling: Self-consistent relating of rupture length, width, average displacement, and moment release, *B Seismol Soc Am*, *100*(5A), 1971-1988.Liu, J., J. Hu, Z. Li, Z. Ma, L. Wu, W. Jiang, G. Feng, and J. Zhu (2021), Complete three-dimensional coseismic displacements due to the 2021 Maduo earthquake in Qinghai Province, China from Sentinel-1 and ALOS-2 SAR images, *SCIENCE CHINA Earth Sciences*, doi:10.1007/s11430-021-9868-9.Liu, J., J. Hu, Z. Li, Z. Ma, L. Wu, W. Jiang, G. Feng, and J. Zhu (2022), Complete three-dimensional coseismic displacements due to the 2021 Maduo earthquake in Qinghai Province, China from Sentinel-1 and ALOS-2 SAR images, *Science China Earth Sciences*, *65*(4), 687-697.Liu, J., J. Hu, Z. Li, J. J. Zhu, Q. Sun, and J. Gan (2018), A Method for Measuring 3-D Surface Deformations With InSAR Based on Strain Model and Variance Component Estimation, *IEEE Trans. Geosci. Remote Sens.*, *56*(1), 239-250, doi:10.1109/TGRS.2017.2745576.Liu, J., J. Hu, W. Xu, Z. Li, J. Zhu, X. Ding, and L. Zhang (2019a), Complete three-dimensional co-seismic deformation fields of the 2016 Central Tottori earthquake by integrating left- and right-looking InSAR with the improved SM-VCE method, *J. Geophys. Res. Solid Earth*, *124*, 12099–12115, doi:10.1029/2018JB017159.Liu, J., J. Hu, W. Xu, Z. Li, J. Zhu, X. Ding, and L. Zhang (2019b), Complete Three-Dimensional Coseismic Deformation Field of the 2016 Central Tottori Earthquake by Integrating Left-and Right-Looking InSAR Observations With the Improved SM-VCE Method, *Journal of Geophysical Research: Solid Earth*, *124*(11), 12099-12115.Liu, J.-H., J. Hu, Z.-W. Li, J.-J. Zhu, Q. Sun, and J. Gan (2017), A method for measuring 3-D surface deformations with InSAR based on strain model and variance component estimation, *IEEE Transactions on Geoscience and Remote Sensing*, *56*(1), 239-250.Meng, L., A. Inbal, and J. P. Ampuero (2011), A window into the complexity of the dynamic rupture of the 2011 Mw 9 Tohoku-Oki earthquake, *Geophys Res Lett*, *38*(7).Michel, R., J. P. Avouac, and J. Taboury (1999), Measuring ground displacements from SAR amplitude images: Application to the Landers Earthquake, *Geophys. Res. Lett.*, *26*(7), 875-878, doi:10.1029/1999GL900138.Poliakov, A. N., R. Dmowska, and J. R. Rice (2002), Dynamic shear rupture interactions with fault bends and off-axis secondary faulting, *Journal of Geophysical Research: Solid Earth*, *107*(B11), ESE 6-1-ESE 6-18.Qiu, Q., E. M. Hill, S. Barbot, J. Hubbard, W. Feng, E. O. Lindsey, L. Feng, K. Dai, S. V. Samsonov, and P. Tapponnier (2016), The mechanism of partial rupture of a locked megathrust: The role of

fault morphology, *Geology*, *44*(10), 875-878.Ren, J., X. Xu, G. Zhang, Q. Wang, Z. Zhang, H. Gai, and W. Kang (2022), Coseismic surface ruptures, slip distribution, and 3D seismogenic fault for the 2021 Mw 7.3 Maduo earthquake, central Tibetan Plateau, and its tectonic implications, *Tectonophysics*, *827*, 229275.Savage, J. (1965), The stopping phase on seismograms, *B Seismol Soc Am*, *55*(1), 47-58.Shi, Q., S. Wei, and M. Chen (2018), An MCMC multiple point sources inversion scheme and its application to the 2016 Kumamoto M w 6.2 earthquake, *Geophys J Int*, *215*(2), 737-752.Shi, Z., and S. M. Day (2013), Rupture dynamics and ground motion from 3-D rough-fault simulations, *Journal of Geophysical Research: Solid Earth*, *118*(3), 1122-1141.Sieh, K., et al. (1993), Near-Field Investigations of the Landers Earthquake Sequence, April to July 1992, *Science*, *260*(5105), 171-176.Templeton, E. L., A. Baudet, H. S. Bhat, R. Dmowska, J. R. Rice, A. J. Rosakis, and C. E. Rousseau (2009), Finite element simulations of dynamic shear rupture experiments and dynamic path selection along kinked and branched faults, *Journal of Geophysical Research: Solid Earth*, *114*(B8).Wang, M., F. Wang, X. Jiang, J. B. Tian, Y. Li, J. B. Sun, and Z. K. Shen (2022a), GPS determined coseismic slip of the 2021 M w7. 4 Maduo, China, earthquake and its tectonic implication, *Geophys J Int*, *228*(3), 2048-2055.Wang, S., C. Song, S. Li, and X. Li (2022b), Resolving co-and early post-seismic slip variations of the 2021 M W 7.4 Madoi earthquake in east Bayan Har block with a block-wide distributed deformation mode from satellite synthetic aperture radar data, *Earth Planet. Phys*, *6*(1), 108-122.Wang, W., L. Fang, J. Wu, H. Tu, L. Chen, G. Lai, and L. Zhang (2021), Aftershock sequence relocation of the 2021 Ms7. 4 Maduo earthquake, Qinghai, China, *Science China Earth Sciences*, *64*(8), 1371-1380.Wegmüller, U., C. Werner, T. Strozzi, A. Wiesmann, O. Frey, and M. Santoro (2016), Sentinel-1 support in the GAMMA software, *Procedia Comput. Sci.*, *100*, 1305-1312, doi:10.5270/Fringe2015.pp70.Wei, S., et al. (2011), Superficial simplicity of the 2010 El Mayor-Cucapah earthquake of Baja California in Mexico, *Nat Geosci*, *4*(9), 615-618, doi:10.1038/ngeo1213.Wells, D. L., and K. J. Coppersmith (1994), New empirical relationships among magnitude, rupture length, rupture width, rupture area, and surface displacement, *B Seismol Soc Am*, *84*(4), 974-1002.Wesnousky (1988), Seismological and structural evolution of strike-slip faults, *Nature*, *335*(6188), 340-343.Wesnousky (2006), Predicting the endpoints of earthquake ruptures, *Nature*, *444*(7117), 358-360.Wesnousky (2008), Displacement and geometrical characteristics of earthquake surface ruptures: Issues and implications for seismic-hazard analysis and the process of earthquake rupture, *B Seismol Soc Am*, *98*(4), 1609-1632.Wright, T. J., B. Parsons, P. C. England, and E. J. Fielding (2004), InSAR observations of low slip rates on the major faults of western Tibet, *Science*, *305*(5681), p.236-239.Yue, H., Z.-K. Shen, Z. Zhao, T. Wang, B. Cao, Z. Li, X. Bao, L. Zhao, X. Song, and Z. Ge (2022), Rupture process of the 2021 M7. 4 Maduo earthquake and implication for deformation mode of the Songpan-Ganzi terrane in Tibetan Plateau, *Proceedings of the National Academy of Sciences*, *119*(23), e2116445119.Zeng, H., S. Wei, and A. Rosakis (2022), A Travel-time Path Calibration Strategy for Back-Projection of Large Earthquakes and Its Application and Validation through the Segmented Super-Shear Rupture Imaging of the 2002 Mw 7.9 Denali

earthquake, *Journal of Geophysical Research: Solid Earth*, e2022JB024359.Zeng, H., S. Wei, and W. Wu (2020), Sources of uncertainties and artefacts in back-projection results, *Geophys J Int*, *220*(2), 876-891.Zhan, Y., M. Liang, X. Sun, F. Huang, L. Zhao, Y. Gong, J. Han, C. Li, P. Zhang, and H. Zhang (2021), Deep structure and seismogenic pattern of the 2021.5. 22 Madoi (Qinghai) M S 7.4 earthquake, *Chinese Journal of Geophysics*, *64*(7), 2232-2252.Zhang, X., W. Feng, H. Du, S. Samsonov, and L. Yi (2022), Supershear rupture during the 2021 MW 7.4 Maduo, China, earthquake, *Geophys Res Lett*, e2022GL097984.Zhu, L., and D. V. Helmberger (1996), Intermediate depth earthquakes beneath the India-Tibet collision zone, *Geophys Res Lett*, *23*(5), 435-438.Zhu, L. P., and L. A. Rivera (2002), A note on the dynamic and static displacements from a point source in multilayered media, *Geophys J Int*, *148*(3), 619-627.